THE *SPITZER* C2D SURVEY OF NEARBY DENSE CORES. XI. INFRARED AND SUBMILLIMETER OBSERVATIONS OF CB130

Hyo Jeong Kim[1], Neal J. Evans II[1], Michael M. Dunham[1,2], Jo-Hsin Chen[1,3], Jeong-Eun Lee[4], Tyler L. Bourke[5], Tracy L. Huard[6], Yancy L. Shirley[7,9], and Christopher De Vries[8]

[1] Department of Astronomy, The University of Texas at Austin, 1 University Station, C1400, Austin, TX 78712-0259, USA; hyojeong@astro.as.utexas.edu
[2] Department of Astronomy, Yale University, 260 Whitney Avenue, New Haven, CT 06511, USA
[3] Jet Propulsion Laboratory, 4800 Oak Grove Drive, Pasadena, CA 91109, USA
[4] Department of Astronomy and Space Science, Astrophysical Research Center for the Structure and Evolution of the Cosmos,
Sejong University, Seoul 143-747, Republic of Korea
[5] Harvard-Smithsonian Center for Astrophysics, 60 Garden Street, Cambridge, MA 02138, USA
[6] Department of Astronomy, The University of Maryland, College Park, MD 20742-2421, USA
[7] Steward Observatory, University of Arizona, 933 North Cherry Avenue, Tucson, AZ 85721, USA
[8] California State University, Stanislaus, One University Circle, Turlock, CA 95382, USA
Received 2010 July 1; accepted 2011 January 4; published 2011 February 11

ABSTRACT

We present new observations of the CB130 region composed of three separate cores. Using the *Spitzer Space Telescope*, we detected a Class 0 and a Class II object in one of these, CB130-1. The observed photometric data from *Spitzer* and ground-based telescopes are used to establish the physical parameters of the Class 0 object. Spectral energy distribution fitting with a radiative transfer model shows that the luminosity of the Class 0 object is 0.14–0.16 $L_\odot$, which is low for a protostellar object. In order to constrain the chemical characteristics of the core having the low-luminosity object, we compare our molecular line observations to models of lines including abundance variations. We tested both ad hoc step function abundance models and a series of self-consistent chemical evolution models. In the chemical evolution models, we consider a continuous accretion model and an episodic accretion model to explore how variable luminosity affects the chemistry. The step function abundance models can match observed lines reasonably well. The best-fitting chemical evolution model requires episodic accretion and the formation of CO_2 ice from CO ice during the low-luminosity periods. This process removes C from the gas phase, providing a much improved fit to the observed gas-phase molecular lines and the CO_2 ice absorption feature. Based on the chemical model result, the low luminosity of CB130-1 is explained better as a quiescent stage between episodic accretion bursts rather than being at the first hydrostatic core stage.

Key words: astrochemistry – infrared: ISM – ISM: individual objects (CB130) – stars: formation – stars: low-mass – submillimeter: ISM

Online-only material: color figures

1. INTRODUCTION

The *Spitzer Space Telescope* Legacy Project, From Molecular Cores to Planet Forming Disks (c2d; Evans et al. 2003), has completed a survey of nearby star-forming regions. It covered five clouds containing 1024 objects classified as young stellar objects (YSOs; Evans et al. 2009). When a dense core forms a central protostar, it develops a luminosity source from the accretion of infalling mass. The accretion luminosity is given as $L_{acc} = G M_* \dot{M}_{acc}/R_*$, where M_* is the mass of the protostar, $\dot{M}_{acc}$ is the mass accretion rate onto the protostar, and R_* is the radius of the protostar. According to the standard model, the mass accretion rate from spherical infall of the envelope is $\dot{M}_{acc} \simeq 2 \times 10^{-6} M_\odot$ yr^{-1} if the infall occurs at the thermal sound speed at 10 K (Shu 1977). With a typical protostellar radius of 3 $R_\odot$, and a mass at the stellar/brown dwarf boundary of 0.08 $M_\odot$, the resulting L_{acc} is 1.6 $L_\odot$. Any luminosity from contraction of the forming star will add to this accretion luminosity, making it a minimum value in the standard model.

In contrast to the predictions, the c2d survey showed that 59% of the 112 embedded protostars (Class 0/I) have luminosity lower than 1.6 $L_\odot$ (Evans et al. 2009), indicating that either

M_* is very small, or $\dot{M}_{acc}$ is lower than expected, or both. This luminosity problem was aggravated by the discovery of Very Low Luminosity Objects (VeLLOs; di Francesco et al. 2007). VeLLOs are defined as embedded protostars with internal luminosity lower than 0.1 $L_\odot$. The internal luminosity of an embedded protostar is the luminosity of the protostar and disk, excluding luminosity from external heating. By using the correlation between 70 μm flux and the internal luminosity of protostars, Dunham et al. (2008) identify 15 VeLLO candidates in the full c2d sample. Several VeLLOs, including L1014-IRS (Young et al. 2004a), L1148-IRS (Kauffmann et al. 2005), L1521F-IRS (Bourke et al. 2006), IRAM 04191-IRS (André et al. 1999; Dunham et al. 2006), L328-IRS (Lee et al. 2009), and L673-7 (Dunham et al. 2010b), have been studied in detail. Among these VeLLOs, IRAM 04191+1522 and L673-7 drive strong molecular outflows (André et al. 1999; Dunham et al. 2006, 2010b). A low accretion luminosity with a significant molecular outflow can imply higher $\dot{M}_{acc}$ in the past (Dunham et al. 2010b).

One possible explanation for the sources with low luminosities combined with strong molecular outflows is that the mass accretion is not a constant process but rather episodic, and the VeLLOs are in quiescent phases between the mass accretion bursts (Kenyon et al. 1990; Enoch et al. 2009; Dunham et al.

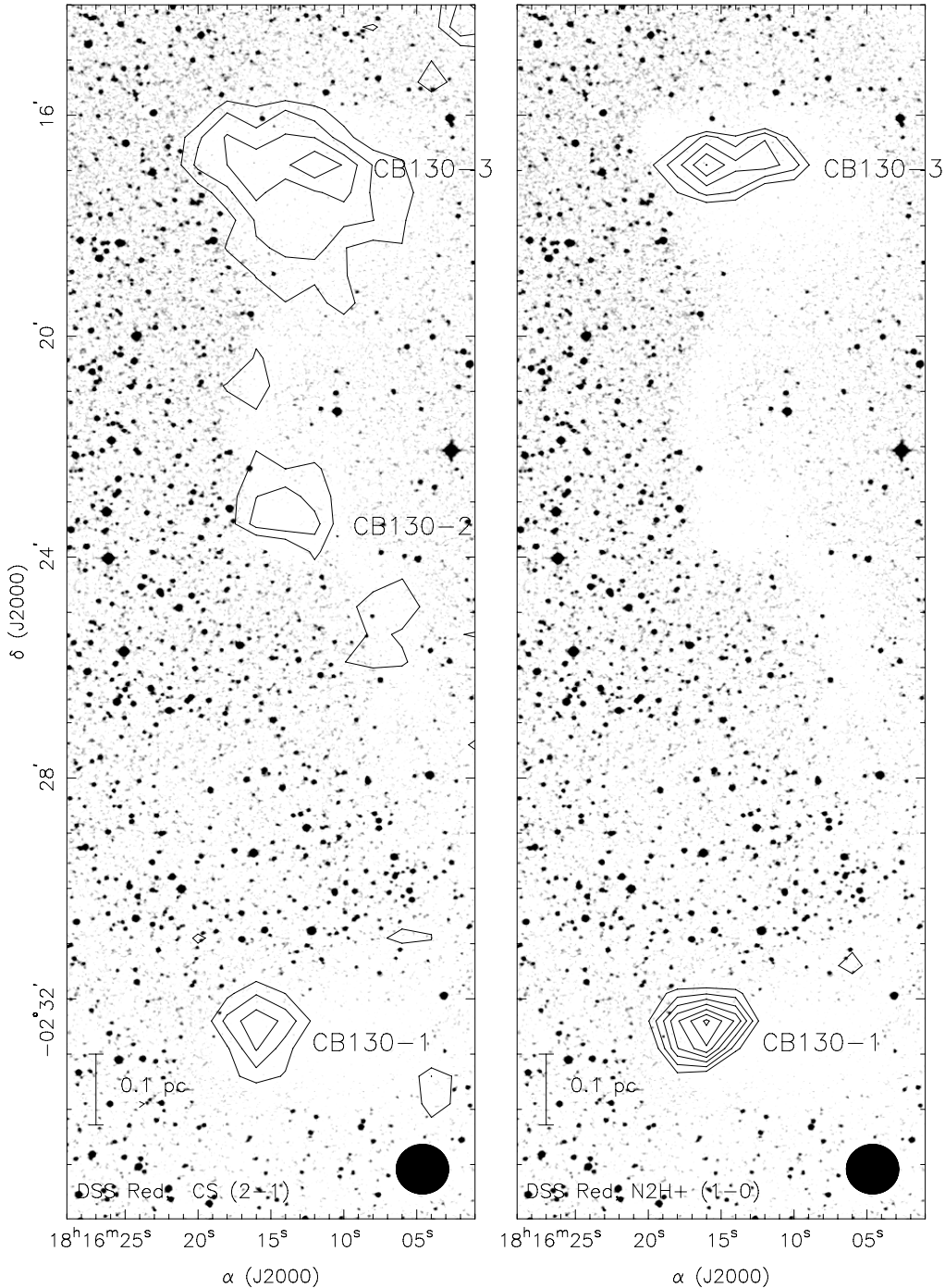[9] Adjunct Astronomer at the National Radio Astronomy Observatory.

Figure 1. DSS *R*-band image (gray scale) with CS (2-1) (left) and N$_2$H$^+$ (1-0) (right) contours from the FCRAO (C. H. De Vries et al. 2011, in preparation). The CS (2-1) contour levels are 0.4, 0.6, and 0.8 times the peak value of 0.32 K km s^{-1}. The N$_2$H$^+$ (1-0) contour levels are 0.3, 0.4, 0.5, 0.6, 0.7, 0.8, and 0.9 times the peak value of 1.37 K km s^{-1}. N$_2$H$^+$ (1-0) emission is not detected from the CB130-2 core. The beam size is shown in the lower right corner of both panels.

2010a). Dunham et al. (2010a) present a set of evolutionary models describing collapse including episodic accretion. The luminosity distribution of YSOs can be matched only when the model includes episodic accretion.

While dust continuum emission can provide the physical structure and evolutionary stage of a core, molecular line observations trace the dynamics and chemistry of the core. The simple empirical models of step function (Lee et al. 2003) and drop function (Jørgensen et al. 2004) abundance profiles have been used to approximate the abundance profiles. The chemical evolution model during protostellar collapse developed by Lee

et al. (2004) has been tested for individual cores, such as B335 (Evans et al. 2005) and L43 (Chen et al. 2009). Using this model, Lee (2007) studied chemical evolution in VeLLOs. The low-luminosity sources can provide chemical laboratories to test the astrochemistry of low-luminosity environments. Because the chemical equilibrium time can be longer than the duration of an accretion burst, the abundance profile may provide a fossil record of previous luminosity bursts.

This paper presents new observations of the CB130 region. With a detailed analysis of *Spitzer*, submillimeter continuum, and molecular line data we will reveal the physical properties
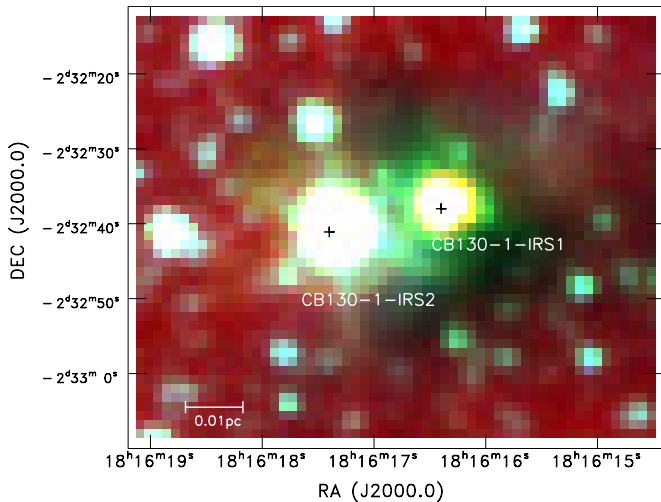
Figure 2. Three-color image of CB130-1 using the cores2deeper IRAC image with IRAC 3.6 μm, 4.5 μm, and 8.0 μm as blue, green, and red, respectively. CB130-1-IRS1 and IRS2 are labeled and marked with black plus signs.

Figure 3. Three-color image composed of near IR band image, with *J* as blue, *H* as green, and *K* as red. The left plus sign indicates CB130-1-IRS2, and the right plus sign is the position of CB130-1-IRS1. The light at the position of CB130-1-IRS1 is mostly scattered light from CB130-1-IRS1. The white arrows indicate the cone shape nebulosity from CB130-1-IRS1 extending toward CB130-1-IRS2.

of this source and use CB130 as a laboratory to study the chemistry in low-luminosity sources. In Section 2, we give a general introduction to CB130. The observations are described in Section 3. Section 4 presents images, photometry, and molecular line data. Section 5 presents dust continuum radiation transfer models used to determine physical parameters. The line modeling with an empirical step function is described in Section 6. The chemical evolution models with different luminosity evolution are presented in Section 7, and we summarize our findings in Section 8.

2. CB130

CB130-1 first appears in the catalog of Clemens & Barvainis (1988), which presents 248 small isolated molecular clouds. Clemens & Barvainis (1988) called the core CB130. Later, Lee & Myers (1999) identified three cores near CB130 and named them CB130-1, CB130-2, and CB130-3, respectively, from south to north. Figure 1 shows the *R*-band image from the Digital Sky Survey (DSS), with CS (left) and N$_2$H$^+$ (right) molecular line contours (C. H. De Vries et al. 2011, in preparation; see Section 3) overlaid. The three cores are clearly identified as separate dark cores in the region. Wu et al. (2007) presented Submillimeter High Angular Resolution Camera II (SHARC-II) 350 μm and 450 μm detections of CB130-1. Dunham et al. (2008) identified an embedded source in CB130-1 with $L_{int} \sim 0.07\,L_\odot$ based on a correlation between the 70 μm flux and the internal source luminosity. However, this result is an estimate and is only good to within a factor of $\sim$2. Recently, Launhardt et al. (2010) presented a survey of low-mass star-forming cores in 32 Bok globules, including CB130-1. They found a faint near-infrared (NIR) source and a very red star in CB130-1, and they identified these as Class 0 and Class II objects, respectively.

CB130 is located in the Aquila Rift cloud, whose galactic coordinates are $20° < l < 40°$ and $-6° < b < +14°$. The local standard of rest (LSR) velocity of the Aquila Rift cloud is 8 km s^{-1} (Dame & Thaddeus 1985), which is similar to the velocity of CB130-1 (see Section 6). Straižys et al. (2003) determined the distance to the Aquila Rift, using extinction methods, to extend between 225 and 310 pc, and the central region at 270 pc. We thus adopt a distance to CB130-1 of 270 pc but note the substantial uncertainty.
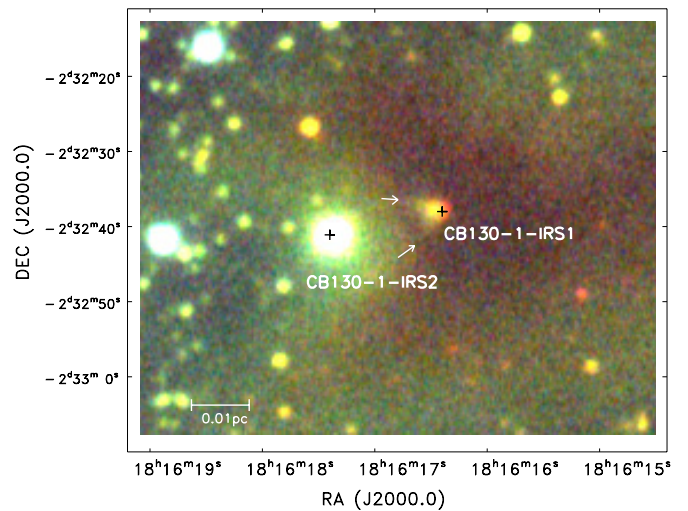
3. OBSERVATIONS

We obtained observational data from various telescopes. All three instruments mounted on *Spitzer* observed CB130-1 in the c2d program: the Infrared Array Camera (IRAC; Fazio et al. 2004), the Infrared Spectrograph (IRS; Houck et al. 2004), and the Multiband Imaging Photometer for SIRTF (MIPS; Rieke et al. 2004). The IRAC images were obtained on 2004 September 2 and 3 (Program ID [PID] 139; c2d; Evans et al. 2003; AOR keys 0005145856 and 0005146368), the IRS spectra were obtained on 2006 April 26 (PID 179; PI: N. J. Evans; AOR key 0015921153), and the MIPS 24 and 70 μm data were obtained on 2004 September 25 (PID 139, AOR key 0009412608, 0009421824).

The IRAC and MIPS images from c2d were reduced by the Spitzer Science Center using the standard pipeline version S13 to produce Basic Calibrated Data (BCD) images. The BCD images are obtained by subtracting the dark and bias levels, and performing flat fielding and sky subtraction. A full explanation of this extra processing data can be found in the documentation of the final delivery of data from the c2d legacy project (Evans et al. 2007).

The IRS data were reduced following the IRS pipeline version S14.0.0, which produces BCD files. IRS BCD files are two-dimensional (2D) spectra, which have been processed including saturation flagging, dark-current subtraction, linearity correction, cosmic ray correction, ramp integration, droop correction, stray light removal or crosstalk correction, and flat-field correction. Detailed explanations about the data delivery can be found in the c2d Spectroscopy Explanatory Supplement (Lahuis et al. 2006).

Spitzer IRAC and MIPS 24 μm images of CB130-1 were also obtained in the *Spitzer* GO-2 program (cores2deeper; PID 20386; PI: P. C. Myers), which obtained deeper images of a sample of cores from the c2d program. IRAC 4 band images were obtained on 2005 September 16 (AOR key 0014606848) and on 2005 September 19 (AOR key 0014607104). MIPS 24 μm image was obtained on 2005 October 5 (AOR key 0014615040). Additional *Spitzer* MIPS images at 24 μm and

3

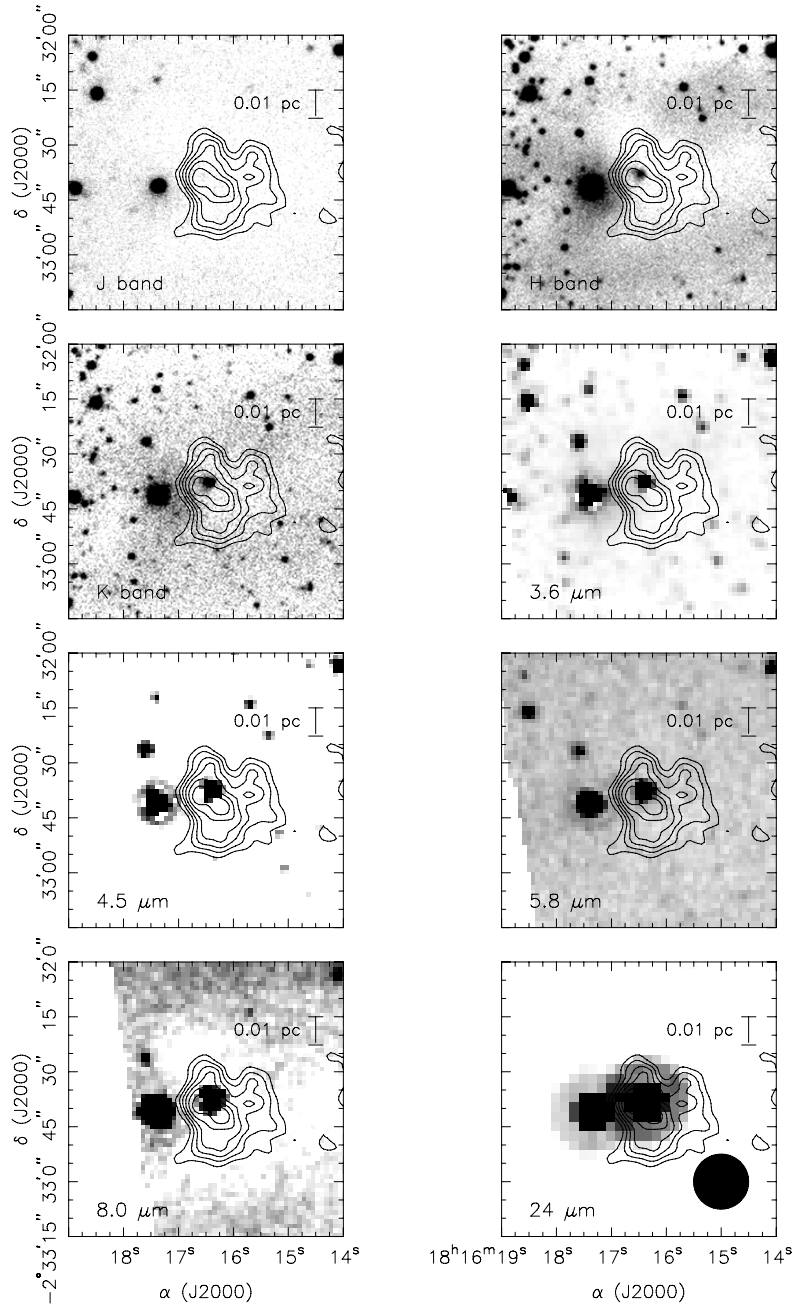**Figure 4.** Photometry images from the different wavelengths. The *J*-, *H*-, and *K*-band images are from ISPI, the 3.6 μm, 4.5 μm, 5.8 μm, and 8.0 μm images are from IRAC, and the 24 μm image is from MIPS. We plot the contours taken from the 850 μm SCUBA. The beam size of SCUBA at 850 μm is shown in the bottom right of the 24 μm panel. The contour levels are 0.5, 0.6, 0.7, 0.8, and 0.9 times the peak value (248 mJy beam^{-1}).

70 μm were obtained along with the 160 μm image on 2007 May 18 (PID 30384; PI: T. L. Bourke; AOR key 0018159616). IRAC images were reduced in the same way as the c2d data. MIPS images from PID 20386 and PID 30384 were reduced using the MIPS Data Analysis Tool (DAT; Gordon et al. 2005). The data reduction process is described in Stutz et al. (2007).

Submillimeter Common User Bolometer Array (SCUBA)[10] observations at 850 μm, taken at the James Clerk Maxwell Telescope (JCMT), were obtained from the CADC archive. The SCUBA jiggle maps were analyzed using the standard

SCUBA User Reduction Facility reduction package and aperture photometry was calibrated using Uranus observations obtained from the same night (see Shirley et al. 2000 for the flux calibration procedure). The beam size at 850 μm is 15″.

NIR observations of CB130-1 were obtained during 2005 March 24–25 using the Infrared Sideport Imager (ISPI) on the 4 m Blanco telescope at the Cerro Tololo Inter-American Observatory (CTIO). Deep observations at *J* and *H* were obtained with 60 s and 30 s exposures, respectively. Deep *K*s observations were obtained with two coadded 10 s exposures. The total exposure times achieved for these deep observations were 9, 76, and 17 minutes at *J*, *H*, and *K*s, respectively. To obtain photometry of most moderately bright stars, which were saturated in these deep observations, shallower 3 s exposures

---
[10] This research used the facilities of the Canadian Astronomy Data Centre operated by the National Research Council of Canada with the support of the Canadian Space Agency.
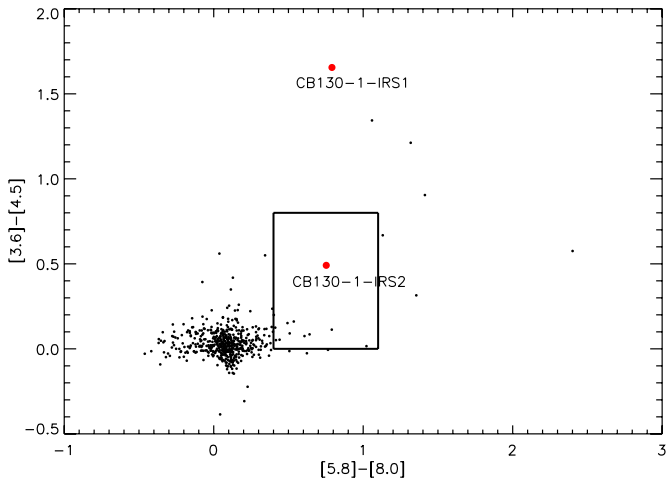
Figure 5. Color–color diagram for the four IRAC bands. The notation [3.6]−[4.5] denotes the magnitude difference, or color, between 3.6 and 4.5 μm. The box indicates the location of Class II sources (Allen et al. 2004). The two YSOs in CB130-1 are clearly redder than the background stars. CB130-1-IRS2 is clearly in the box where Class II sources are found, whereas IRS1 is not. The black dots are classified as stars (those with colors near zero) or galaxies (those in the Class II or Class I regions).

(A color version of this figure is available in the online journal.)

were obtained. The individual images were reduced using IRAF and IDL procedures following the standard method, as described in Huard et al. (2006), to construct the final stacked images at J, H, and Ks. Sources were identified in these final images and 1″2 radius aperture photometry was derived using PhotVis, version 1.09 (Gutermuth et al. 2004), an IDL GUI-based aperture photometry tool that uses standard DAOPHOT packages (Landsman 1993). Finally, the photometry was calibrated by comparison with published photometry of sources listed in the Two Micron All Sky Survey (2MASS) catalog. The average seeing during the J observations was ∼1″3, and ∼1″1 during the H and Ks observations.

The molecular line spectral data were obtained from several telescopes (see Tables 3–5). The majority of the lines were observed at the Caltech Submillimeter Observatory (CSO)[11] from 2005 to 2009. For the data obtained between 2005 and 2007, we used an acousto-optic spectrometer (AOS), with 1024 channels and 50 MHz bandwidth. For the 2008–2009 data, we used a fast Fourier transform spectrometer with 8192 channels and 500 MHz bandwidth. We used the 230 GHz heterodyne receiver for all the lines except H_2D^+ ($J_{K_{-1}K_{+1}} = 1_{1,0} \rightarrow 1_{1,1}$), for which we used the 345 GHz receiver. The position switched scans were taken when the optical depth at 225 GHz was between 0.1 and 0.2. The calibration uncertainty is about 10%. N_2H^+ ($J = 1 \rightarrow 0$) and CS ($J = 2 \rightarrow 1$) maps were obtained at the Five College Radio Astronomy Observatory (FCRAO; C. H. De Vries et al. 2011, in preparation), and N_2H^+ ($J = 1 \rightarrow 0$) data were obtained from the Arizona Radio Observatory (ARO) on 2007 March. We reduced the molecular line data from the CSO, FCRAO, and ARO 12 m telescope using CLASS.[12]

4. RESULTS

4.1. The Images and Photometry

A three-color image of CB130-1 using cores2deeper IRAC data is presented in Figure 2, with 3.6 μm as blue, 4.5 μm
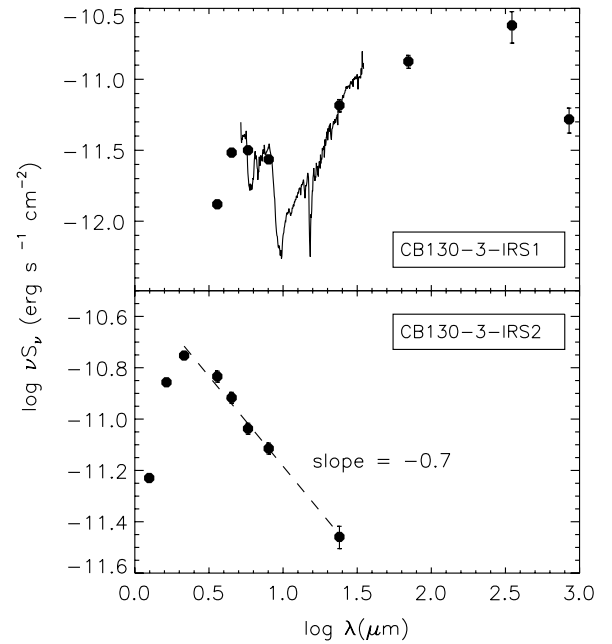

Figure 6. SEDs of CB130-1-IRS1 (upper panel) and CB130-1-IRS2 (lower panel). The photometry data from ISPI, IRAC, MIPS, SHARC-II, and SCUBA are plotted as filled circles with error bars. The IRS spectrum of CB130-1-IRS1 is plotted as a solid line. CB130-1-IRS1 has a generally rising infrared SED, and peaks at 350 μm. CB130-1-IRS2 is not detected longward of 24 μm. The dashed line in the lower panel is the slope of the SED from 2.17 μm to 24 μm. The slope is −0.69, which indicates that CB130-1-IRS2 is a Class II object.

as green, and 8.0 μm as red. Two YSOs are identified in these data based on their positions in various color–color and color–magnitude diagrams (Harvey et al. 2007). These two YSOs are 15″ apart, which corresponds to 4100 AU at a distance of 270 pc (Straižys et al. 2003). We name the western source ($\alpha = 18^h 16^m 16\overset{s}{.}4$, $\delta = −02°32′38″0$ [J2000]) CB130-1-IRS1 and the eastern source ($\alpha = 18^h 16^m 17\overset{s}{.}4$, $\delta = −02°32′41″1$ [J2000]) CB130-1-IRS2 and label these sources in Figure 2.

Figure 3 shows a three-color image of CB130-1 using the NIR data with J as blue, H as green, and Ks as red. Both YSOs are detected and labeled in the figure. Cone-shaped nebulosity extends from CB130-1-IRS1 toward CB130-1-IRS2, as marked by arrows in the figure. Similar nebulosity is also observed in L1014 (Huard et al. 2006) and is indirect evidence of an outflow. However, we mapped the CB130-1 region with CO ($J = 2 \rightarrow 1$) at the CSO and found no significant evidence of outflowing gas.

Figure 4 shows 850 μm contours overlaid on the 1.25–24 μm NIR and *Spitzer* images. The 850 μm data probes the envelope since dust emission from the envelope becomes optically thin at long wavelengths. The 850 μm contours peak at CB130-1-IRS1 and avoid CB130-1-IRS2. CB130-I-IRS2 is brighter at all wavelengths up to 8 μm, but CB130-1-IRS1 is stronger at 24 μm. These facts support the conclusion by Launhardt et al. (2010) that CB130-1-IRS1 is younger and more embedded than CB130-1-IRS2.

A color–color diagram constructed from the IRAC photometry for all sources detected in the *Spitzer* images of the CB130 region is plotted in Figure 5. Sources inside the box are generally Class II sources (Allen et al. 2004). The two sources in CB130-1 are clearly redder than background stars. The color–color diagram shows that CB130-1-IRS1 and CB130-1-IRS2 are in different phases of evolution. CB130-1-IRS2 is clearly in the
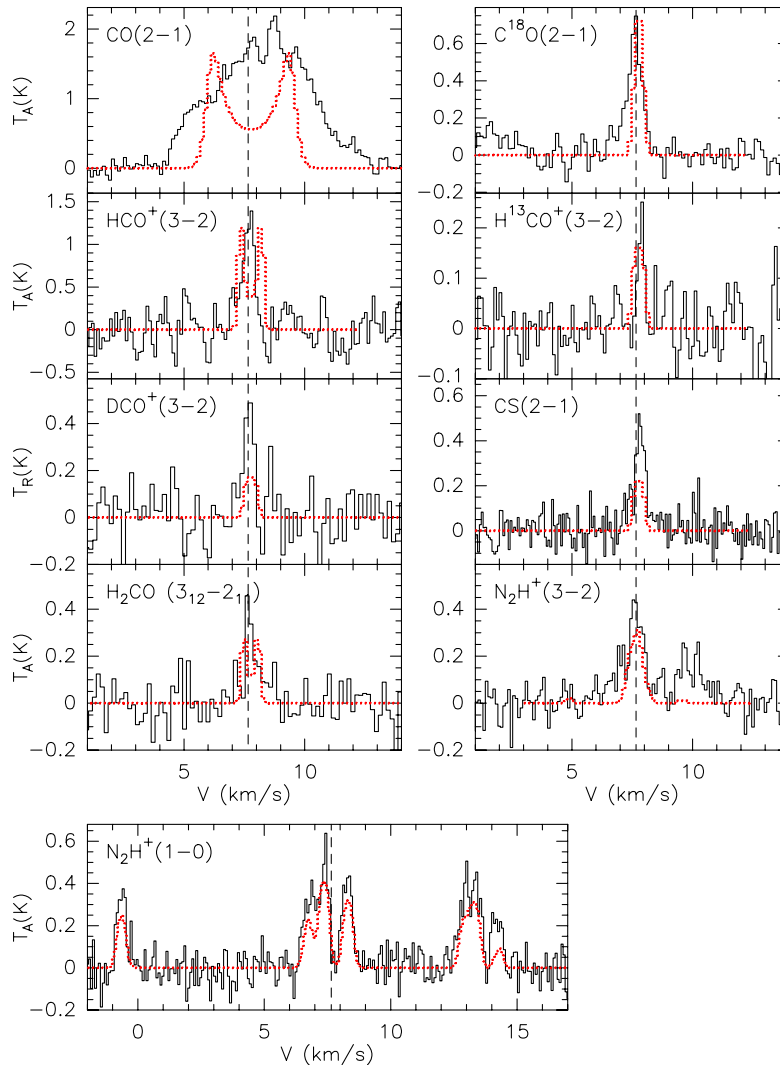

Figure 7. Observed molecular lines of CB130-1 and line modeling results for step function abundances (see Section 6). The observed data are plotted as solid lines. The vertical dashed lines are line centers determined by averaging the LSR velocity of optically thin lines. The modeled data are plotted as dotted lines. The modeled $C^{18}O$, $H^{13}CO$, N_2H^+, and CS lines show a good fit with the observed lines, while CO and HCO^+ lines show a poor fit with the observed lines. CO is confused by the wing component; modeled lines of HCO^+ and H_2CO show self-absorption features.

(A color version of this figure is available in the online journal.)

region of Class II sources. The sources for which either the [3.6]–[4.5] color is greater than 0.8 mag or the [5.8]–[8.0] color is greater than 1.1 mag are all faint and classified as galaxies except for CB130-1-IRS1 (Harvey et al. 2007). Since no YSO candidates in CB130-2 and CB130-3 were detected with CTIO and *Spitzer*, we will concentrate on CB130-1 for the remainder of the paper.

4.2. CB130-1-IRS1

The photometric data for CB130-1-IRS1 are given in Table 1, which lists wavelength, flux density, uncertainty in flux density, aperture diameter, and telescope. At 3.6–24 μm, we list the flux averaged between the c2d and cores2deeper images, weighted by the inverse of the uncertainties. The spectral energy distribution (SED) is plotted in the upper panel of Figure 6, including the IRS spectrum, which clearly contains 10 μm silicate and 15.2 μm CO_2 absorption features. Using the 15.2 μm CO_2 absorption feature, we can derive the CO_2 abundance toward CB130-1-IRS1. The continuum for

the spectrum is constructed by fitting a first-order polynomial to the ranges 12–14.7 and 16.2–18 μm. After subtracting the continuum, we calculated the CO_2 column density from $N(CO_2)= \int \tau(\nu)d\nu/A$, where $\tau(\nu)$ is an optical depth, ν is the wave number (cm^{-1}), and $A = 1.1 \times 10^{-17}$ (cm) is the band strength (Gerakines et al. 1995). We find $\int \tau(\nu)d\nu = 28 \pm 0.4$ cm^{-1} and $N(CO_2)= (2.6 \pm 0.05) \times 10^{18}$ cm^{-2}. We calculated the H_2 column density using 850 μm data. Using Equation (6) in Lee et al. (2003), we have $N(H_2)= 4.5 \times 10^{22}$ cm^{-2}. From $N(CO_2)$ and $N(H_2)$, the abundance of CO_2 ice is 5.8×10^{-5}, which requires a substantial fraction of the carbon.

Based on the observed SED, we can calculate standard observational signatures including L_{bol}, T_{bol}, and $L_{bol}/L_{(>350\,\mu m)}$. We calculate L_{bol} by integrating the flux over all wavelengths using the average of the results obtained from midpoint and prismoidal integration methods. T_{bol} is the temperature of a blackbody having the same flux-weighted mean frequency as the source and is calculated following Myers & Ladd (1993). $L_{(>350\,\mu m)}$ is the luminosity emitted at $\lambda > 350$ μm.
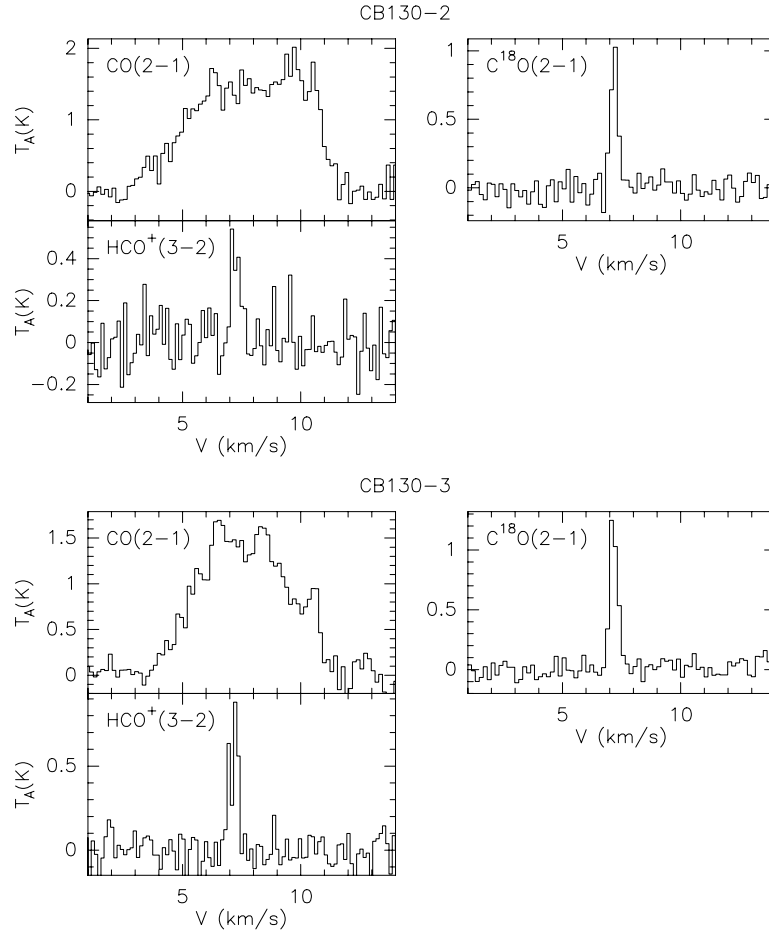
Figure 8. Observed molecular lines of CB130-2 and CB130-3. The parameters and descriptions are in Tables 4 and 5.

Table 1
Photometry of CB130-1-IRS1

λ (μm)	$S_\nu(\lambda)$ (mJy)	σ (mJy)	Aperture Diameter (arcsec)	Telescope
1.25	<0.736	. . .	. . .	CTIO
1.64	0.088	0.002	2	CTIO
2.15	<1.27	. . .	. . .	CTIO
3.6	1.58	0.08	1.7	*Spitzer*
4.5	4.57	0.23	1.7	*Spitzer*
5.8	6.12	0.31	1.9	*Spitzer*
8.0	7.28	0.36	2.0	*Spitzer*
24.0	52.4	5.2	6.0	*Spitzer*
70.0	312	32	50	*Spitzer*
160.0	5840	1700	100	*Spitzer*
350.0	2800	700	40	CSO
850.0	1480	296	120	JCMT

Note. The 350 μm continuum SHARC-II data are presented by Wu et al. (2007).

CB130-1-IRS1 has $L_{bol} = 0.23 \pm 0.03\,L_\odot$, $T_{bol} = 59 \pm 1.6$ K, and $L_{bol}/L_{(>350\,\mu m)} = 9.1$. $L_{bol}/L_{(>350\,\mu m)}$ is used to distinguish Class 0 from Class I sources. The pre-protostellar core/Class 0 transition occurs around $L_{bol}/L_{(>350\,\mu m)} \sim 35$ and the Class 0/I transition occurs at $L_{bol}/L_{(>350\,\mu m)} \sim 175$ (Young & Evans 2005). Since $L_{bol}/L_{(>350\,\mu m)}$ is less than 35, we would guess that CB130-1 is in the pre-protostellar core stage from these criteria, but CB130 clearly contains embedded sources. Another criterion to define a Class 0 object is the bolometric temperature of the source. Class 0 and I objects are divided at $T_{bol} = 70$ K (Chen et al. 1995); thus, CB130-1-IRS1 is classified as a Class 0 source based on T_{bol}.

The bolometric luminosity includes the luminosities of the embedded object, the disk, and the interstellar radiation field (ISRF), which can add several tenths of an $L_\odot$ to L_{bol} (Evans et al. 2001). The luminosity of the internal source can be estimated in two ways. First, assuming that all emission at $\lambda \geqslant 100\,\mu$m arises from external heating, L_{int} can be calculated by integrating the flux at $\lambda \leqslant 100\,\mu$m, giving $L_{int} \sim 0.056\,L_\odot$. Alternatively, we can estimate L_{int} by applying the relation between the flux at 70 μm, normalized to 140 pc, and the L_{int} found by Dunham et al. (2008), giving $L_{int} \sim 0.07\,L_\odot$. These two estimates indicate that CB130-1-IRS1 is in any case a low-luminosity object and may be a VeLLO. However, they are only rough estimates; radiative transfer models of CB130-1 are required to reliably determine the physical properties of the internal source (Section 5).

Assuming that the core is optically thin at submillimeter wavelengths, the envelope mass can be estimated from $M = \frac{S_\nu D^2}{B_\nu(T_d)\kappa_\nu}$, where S_ν is the flux density at 850 μm, D is the distance to the object, $B_\nu(T_d)$ is the blackbody function, and κ_ν is the opacity of gas and dust at 850 μm (Young et al. 2003). Pontoppidan's dust model (K. M. Pontoppidan et al. 2011, in preparation) gives $\kappa_\nu = 1.02 \times 10^{-2}$ cm^{-1} g^{-1} and $\kappa_\nu = 1.8\times10^{-2}$ cm^{-1} g^{-1} for OH5 dust (Ossenkopf & Henning 1994). If we assume the core is isothermal at $T_d = 10$ K, the estimated envelope mass within a 120$''$ diameter aperture (radius of 16,200 AU) is 3.5 $M_\odot$ with the Pontoppidan model, and 2.0 $M_\odot$ with the OH5 model. These estimates will be refined later.
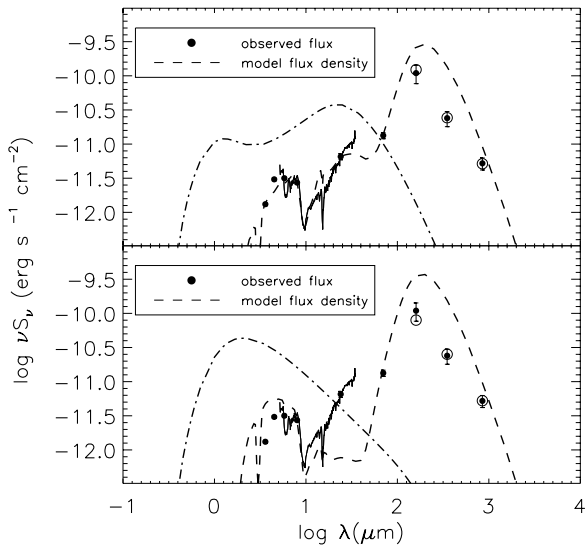
Figure 9. Photometry data and the best-fit 1D radiative transfer model result for CB130-1-IRS1. The photometry data are plotted as filled circles. The data from the IRS is plotted as a solid line. The dash-dotted line is the input SED from the internal source. The final SED is plotted as the dashed line. The aperture size convolved SED is marked with open circles at wavelengths longer than 100 μm. The model parameters are $T_s = 3000$ K, $L_{int} = 0.16\,L_\odot$, and $R_{in} = 350$ AU. The lower panel indicates the radiative transfer modeling result with a passive disk model. With a temperature distribution of a passive disk model, we cannot fit the 24 μm data.

4.3. CB130-1-IRS2

The photometric data for CB130-1-IRS2 are given in Table 2. At 3.6–24 μm, we list the flux averaged between the c2d and cores2deeper images, weighted by the inverse of the uncertainties.

The SED of CB130-1-IRS2 is plotted in the lower panel of Figure 6. CB130-1-IRS2 is not detected at $\lambda > 24\,\mu$m. The slope of the SED of CB130-1-IRS2 from 2.17 μm to 24 μm is −0.7, which indicates that CB130-1-IRS2 is a Class II object (Greene et al. 1994). We can estimate the bolometric luminosity of the source by integrating the SED. The bolometric luminosity of CB130-1-IRS2 is $L_{bol} = 0.071 \pm 0.003\,L_\odot$ and the bolometric temperature is $T_{bol} = 1150 \pm 15$ K. These values of L_{bol} and T_{bol} are not corrected for extinction along the line of sight and are thus lower limits to the intrinsic values.

4.4. The Molecular Line Data

Molecular line observations can trace the dynamics in the core, such as infall, rotation, and outflow. The observed molecular lines for CB130-1, CB130-2, and CB130-3 are summarized in Tables 3, 4, and 5, respectively. The detected molecular lines are plotted in Figure 7 as solid lines. Toward CB130-2, the detected molecular lines are plotted in the upper three panels in Figure 8. Toward CB130-3, the detected lines are plotted in the lower three panels in Figure 8.

In the following section, we will focus on CB130-1-IRS1, since the source is a deeply embedded Class 0 object. We will find the internal luminosity and chemical properties of the source.

5. RADIATIVE TRANSFER MODEL

As discussed above, a detailed radiative transfer model is required to accurately determine the internal luminosity of CB130-1-IRS1. The internal luminosity will determine whether

Table 2
Photometry of CB130-1-IRS2

λ (μm)	$S_\nu(\lambda)$ (mJy)	σ (mJy)	Aperture Diameter (arcsec)	Telescope
1.25	2.46	0.005	2	CTIO
1.64	7.59	0.007	2	CTIO
2.15	12.7	0.0	2	CTIO
3.6	17.6	0.9	1.7	*Spitzer*
4.5	18.2	0.9	1.7	*Spitzer*
5.8	17.8	0.9	1.9	*Spitzer*
8.0	20.5	1.0	2.0	*Spitzer*
24.0	27.8	2.8	6.0	*Spitzer*

the source is a VeLLO or not. This section describes 1D and 2D models of this source. These models trace the radiation from a source in a dusty region, including scattering, absorption, and re-emission by the dust and generate model SEDs that can be compared to the observations.

The 1D models provide one estimate of the internal luminosity and a spherical model that is needed for analyzing the molecular lines. The 2D models provide an alternative estimate of the internal luminosity and a better fit to the SED, at the expense of having more free parameters.

5.1. One-dimensional Radiative Transfer Models

We modeled CB130-1-IRS1 with the 1D radiative transfer code, DUSTY (Ivezic et al. 1999). DUSTY calculates the dust temperature profile and SED of a protostar embedded in a dense core. The parameters of the model divide into those associated with the envelope, or core, and those associated with the internal source.

The envelope is characterized by the outer radius, inner radius, density distribution, dust properties, and external radiation field. The outer radius of the envelope is not well constrained by the radiative transfer modeling as long as it is large enough to include all the emission. We fix the outer radius at 35,000 AU, based on the angular size of CB130-1 ($3'.0 \times 1'.3$; Lee & Myers 1999). The inner radius (R_{in}) will be a free parameter. We assume a power-law radial density distribution for the envelope ($n = n_0(r/r_0)^{-\alpha}$), where n_0 is the density at a fiducial radius, r_0. The value of n_0 was constrained to match the long-wavelength emission, and $\alpha = 1.8 \pm 0.2$ was constrained to match the radial intensity profile. See Shirley et al. (2002) for an explanation of this method.

We use the Pontoppidan dust opacity model (K. M. Pontoppidan et al. 2011, in preparation). The envelope is heated by both the embedded source and the ISRF described by Evans et al. (2001). The ISRF can vary in strength and is modified by extinction by a surrounding low-density envelope. To constrain the ISRF, we used an initial model of the envelope and modeled the CO ($J = 2 \rightarrow 1$) line, since the CO ($J = 2 \rightarrow 1$) line is sensitive to the UV part of the ISRF, and thus the extinction. The best-fit value for the UV part of ISRF is $G_0 = 4.5 \times 10^{-3}$, corresponding to $A_V = 3$. We will discuss this in Section 6. With these dust properties, the density normalization (n_0) yields the total mass of the model envelope within 35,000 AU to be 5.3 $M_\odot$. This mass depends only slightly on the best-fitting parameters for luminosity and inner radius, as long as they are close to the best-fit values. Within 16,200 AU (the size used to estimate the observed mass in Section 4.2), the model contains a mass of 2.2 $M_\odot$, slightly less than the isothermal calculation within that radius.

Table 3
Observation Parameters and Molecular Line Data for CB130-1

Line	Frequency (GHz)	η_{mb}	Beam Size (arcsec)	$\int T_A^* dv$ (K km s^{-1})	v_{LSR} (km s^{-1})	Δv (km s^{-1})	T_A^* (K)	Telescope
CO 2-1	230.537970	0.7	33	9.38	8.27	4.73	1.86	CSO
C^{17}O 2-1	224.714368	0.8	34	. . .	. . .	. . .	<0.14	CSO
C^{18}O 2-1	219.560352	0.8	35	0.48	7.61	0.71	0.64	CSO
HCO$^+$ 3-2	267.557620	0.7	29	0.82	7.67	0.60	1.3	CSO
DCO$^+$ 3-2	216.112605	0.7	36	0.26	7.68	0.47	0.53	CSO
H^{13}CO$^+$ 3-2	260.255339	0.8	30	0.09	7.78	0.49	0.17	CSO
N$_2$H$^+$ 3-2	279.511701	0.7	27	0.45	7.62	0.88	0.10	CSO
N$_2$H$^+$ 1-0	93.173700	0.6	70	2.27	7.35	1.07	0.99	ARO
N$_2$H$^+$ 1-0	93.176258	0.5	54	1.30	7.43	0.44	0.38	FCRAO
CS 2-1	97.980953	0.5	54	0.29	7.78	0.54	0.43	FCRAO
N$_2$D$^+$ 3-2	231.321635	0.7	33	. . .	. . .	. . .	<0.24	CSO
H$_2$D$^+$ 1,1,0–1,1,1	372.421340	0.7	23	. . .	. . .	. . .	<0.29	CSO
H$_2$CO3$_{12}$ − 2$_{11}$	225.697787	0.7	34	0.21	7.74	0.53	0.37	CSO

Table 4
Observing Parameters and Molecular Line Data for CB130-2

Line	Frequency (GHz)	η_{mb}	Beam Size (arcsec)	$\int T_A^* dv$ (K km s^{-1})	v_{LSR} (km s^{-1})	Δv (km s^{-1})	T_A^* (K)	Telescope
CO 2-1	230.537970	0.7	33	10.1	7.99	5.54	1.72	CSO
C^{18}O 2-1	219.560352	0.8	35	0.40	7.19	0.56	1.04	CSO
HCO$^+$ 3-2	267.557620	0.7	29	0.23	7.23	0.47	0.47	CSO
N$_2$H$^+$ 3-2	279.511701	0.7	27	. . .	. . .	. . .	<0.13	CSO
N$_2$D$^+$ 3-2	231.321635	0.7	33	. . .	. . .	. . .	<0.30	CSO
N$_2$H$^+$ 1-0	93.176258	0.5	54	. . .	. . .	. . .	<0.24	FCRAO
CS 2-1	97.980953	0.5	54	0.32	7.38	0.52	0.58	FCRAO

Table 5
Observing Parameters and Molecular Line Data for CB130-3

Line	Frequency (GHz)	η_{mb}	Beam Size (arcsec)	$\int T_A^* dv$ (K km s^{-1})	v_{LSR} (km s^{-1})	Δv (km s^{-1})	T_A^* (K)	Telescope
CO 2-1	230.537970	0.7	33	7.77	7.59	4.51	1.62	CSO
C^{18}O 2-1	219.560352	0.8	35	0.55	7.16	0.40	1.28	CSO
HCO$^+$ 3-2	267.557620	0.7	29	0.36	7.18	0.48	0.70	CSO
N$_2$H$^+$ 3-2	279.511701	0.7	27	. . .	. . .	. . .	<0.13	CSO
N$_2$D$^+$ 3-2	231.321635	0.7	33	. . .	. . .	. . .	<0.15	CSO
N$_2$H$^+$ 1-0	93.176258	0.5	54	0.59	7.90	0.23	0.41	FCRAO
CS 2-1	97.980953	0.5	54	0.42	7.39	0.83	0.54	FCRAO

The internal source is characterized by an internal luminosity (L_{int}) and a stellar temperature (T_s). The luminosity of the disk is included in the model, but the disk luminosity is not easily separable from the stellar luminosity, so we treat the sum as the free parameter: $L_{int} = L_s + L_{disk}$. The emission from the disk is averaged over all inclination angles and added to the input spectrum (Butner et al. 1994). The 24 μm photometry data constrains the disk parameters. The surface density profile of the model disk follows $\Sigma(r) \propto r^{-p}$ with $p = 1.5$. We choose a disk temperature distribution following $T(r) \propto r^{-q}$. When the disk is a flat passive disk, $q = 0.75$. For the flat passive disk, all the luminosity comes from the re-radiation from the central star. A flat passive disk produces less 24 μm emission than observed (lower panel of Figure 9). We varied the index of the temperature distribution until it fitted the observed 24 μm data. The best-fit power-law index of the disk temperature distribution is $q = 0.4$, which corresponds to a flared disk (Chiang & Goldreich 1997). The disk temperature distribution is also less steep than the flat disk case if the disk has an intrinsic luminosity source, such as accretion and back warming from the envelope in addition to radiation from the central star.

DUSTY calculates the radiative transfer from the internal source and the external radiation field. Then, the OBSSPHere (Shirley et al. 2002) program, which convolves the model with a beam, is applied to the DUSTY result to convert models into observed flux densities and model radial profiles at wavelength longer than 100 μm. The model parameters are constrained by the observed SED and the observed radial intensity profile at 850 μm.

We tested a grid of models to obtain the best-fit free parameters. After the constraints described above, the remaining free parameters are T_s, L_{int}, and R_{in}. We calculated the reduced χ^2 to quantify the quality of the fit. The data used to constrain the model covers 3.5 μm $\leqslant \lambda \leqslant$ 850 μm, with a total of nine points of photometry data. We do not include H-band photometry data, because H-band flux comes mainly from scattered photons in the envelope, and DUSTY modeling does not properly treat scattering at short wavelengths. Also, we focus on the photometric data and check the IRS spectrum only for consistency. We have nine data points and three free parameters, so the degree of freedom of reduced χ^2 is 6.

The χ^2 plots are in Figure 10. When we plot Figure 10, we hold fixed the other two parameters at the values with
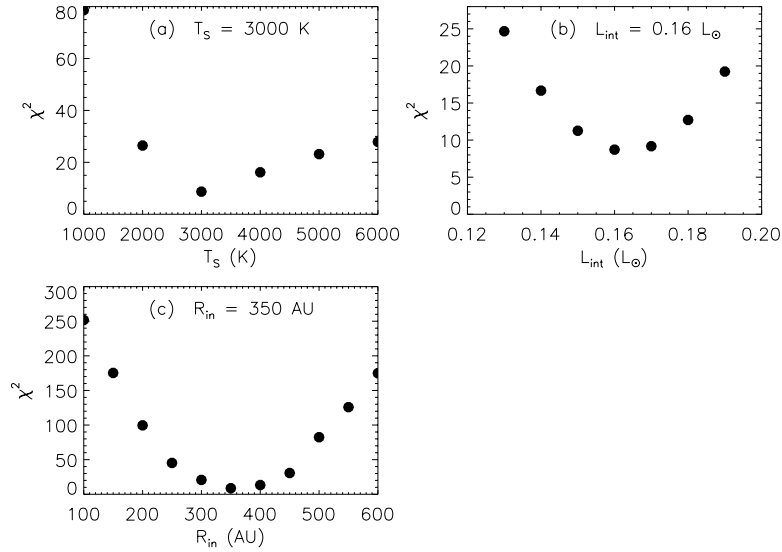
Figure 10. χ^2 plots for a grid of 1D radiative transfer models. Panel (a) is χ^2 vs. T_s, with L_{int} and R_{int} held fixed at 0.16 $L_\odot$ and 350 AU, respectively. The smallest χ^2 is at $T_s = 3000$ K. Panel (b) is χ^2 vs. L_{int}, with T_s and R_{in} held fixed at 3000 K and 350 AU. The smallest χ^2 is at $L_{int} = 0.16 L_\odot$. Panel (c) is χ^2 vs. R_{in}, with T_s and L_{int} held fixed at 3000 K, and 0.16 $L_\odot$. The smallest χ^2 is at $R_{in} = 350$ AU.
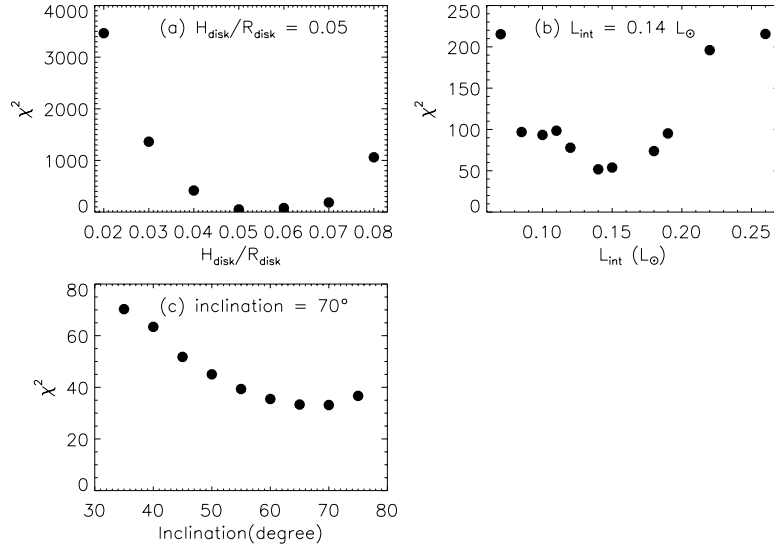
Figure 11. χ^2 plots for a grid of 2D radiative transfer models. Panel (a) is χ^2 vs. H_{disk}/R_{disk}, with $L_{int} = 0.14 L_\odot$, and an inclination angle of 45°. The inclination angle of 0° is face-on. The smallest χ^2 is at $H_{disk}/R_{disk} = 0.05$. Panel (b) is χ^2 vs. L_{int}, with $H_{disk}/R_{disk} = 0.05$, and an inclination angle of 45°. The smallest χ^2 is at $L_{int} = 0.14 L_\odot$. Panel (c) is χ^2 vs. inclination angle, with $H_{disk}/R_{disk} = 0.05$, and $L_{int} = 0.14 L_\odot$. The smallest χ^2 is at an inclination angle of 70°.

the smallest χ^2 values. We plot in panel (a) of Figure 10 varying T_s from 1000 K to 7000 K. The value of T_s does not critically affect the modeled SED, since all the stellar photons are reprocessed by dust close to the star. The lowest χ^2 is found at $T_s = 3000 \pm 500$ K. Panel (b) is χ^2 obtained by varying $L_{int} = L_s + L_{disk}$. The best fit is found at $L_{int} = 0.16 \pm 0.005 L_\odot$. The L_{int} is a little higher than the VeLLO criterion, but much lower than the accretion luminosity calculated from the mass accretion rate in Shu's (1977) model. Panel (c) is the χ^2 plot varying R_{in}. The inner radius of the envelope controls the optical depth. When the optical depth increases, the flux density decreases at short wavelengths because dust absorbs energy at short wavelengths and re-emits at long wavelengths. The best-fit inner radius is $R_{in} = 350 \pm 25$ AU, which gives $\tau = 0.22$ at 100 μm.

The resulting model SED is plotted in Figure 9. The flux density at wavelengths longer than 100 μm comes mainly from the envelope. Since the envelope is bigger than the aperture size, the modeled flux density is higher than the observations. To compare to observations, we used OBSSPHere to convolve the model with the aperture that was used for the photometry. The convolved model data are marked with open circles in Figure 9. The SED shows a good fit to the observed data at 24 μm, 70 μm, 160 μm, 350 μm, and 850 μm. However, the modeled SED shows a 24–30 μm turnover and shallow 15.2 μm CO_2 feature, which is not an ideal fit to the IRS spectrum.

5.2. Two-dimensional Radiative Transfer Models

The best-fit result with the 1D radiative transfer model fails to fit the IRS spectrum at wavelength 24–30 μm. The flux density in the mid-infrared (MIR) region mainly comes from the disk emission. There are limitations to models of disks averaged over all inclinations. For a more realistic explanation of the MIR spectrum, we used the 2D axisymmetric Monte
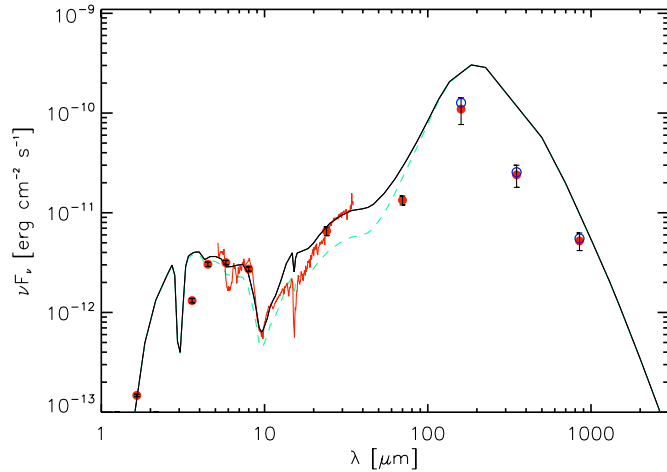
Figure 12. SEDs obtained from the 2D radiative transfer modeling. The red filled circles are the photometry data from the *Spitzer*, CSO, and JCMT, and the red solid line is the spectrum from the *Spitzer* IRS. The black solid line is the SED obtained from the model at an inclination angle of 50°. The blue open circles are flux densities at wavelengths where the source model has been convolved with the aperture used for measuring fluxes. The green dashed line shows the model SED for an inclination angle of 70° for comparison.

(A color version of this figure is available in the online journal.)

Carlo (MC) code, RADMC (Dullemond & Dominik 2004). The RADMC program solves the radiative transfer equation in 2D circumstellar dust configurations. Once a dust temperature distribution is determined, RAYTRACE is used to create smooth SEDs for various inclination angles. As with the 1D models, we use some constraints to determine some parameters before running a fine grid; this reduces the multi-dimensional fitting problem to a manageable size.

We used the same dust opacity and ISRF models used for the 1D model. For the 2D model envelope, we used a slowly rotating cloud core with a small angular momentum (Terebey et al. 1984, hereafter TSC). The initial state of the TSC model is a singular isothermal sphere, with density proportional to r^{-2}. As the core evolves, the collapse of the isothermal sphere includes the effects of an initially uniform and slow rotation. The density of the TSC envelope is determined by the initial angular velocity, Ω_0, and the time, t. We set $\Omega_0 = 10^{-14}\,\mathrm{s}^{-1}$, which is the value used in the TSC model. As t increases, the infall radius gets larger and the density distribution gets flattened. The best-fit density distribution is constrained, as described for the 1D model, to correspond to $t = 35{,}000$ years. We use the inner radius and the outer radius as 350 AU and 35,000 AU, respectively, which were determined by the 1D model and the core size. The mass of the envelope that matches the long-wavelength emission is 5.5 $M_\odot$, only slightly larger than the 1D model estimate in Section 5.1.

For the disk density structure, we use the axisymmetric flared disk (Dullemond et al. 2001; Whitney et al. 2003; Pontoppidan et al. 2007b). The central disk structure is as follows:

$$\rho(R,z) = \frac{\Sigma(R)}{H_p(R)\sqrt{2\pi}}\exp\left[-\frac{z^2}{2H_p(R)^2}\right], \qquad (1)$$

where the surface density Σ is

$$\Sigma(R) = \Sigma_{\mathrm{disk}}\left(\frac{R}{R_{\mathrm{disk}}}\right)^{-p} \qquad (2)$$
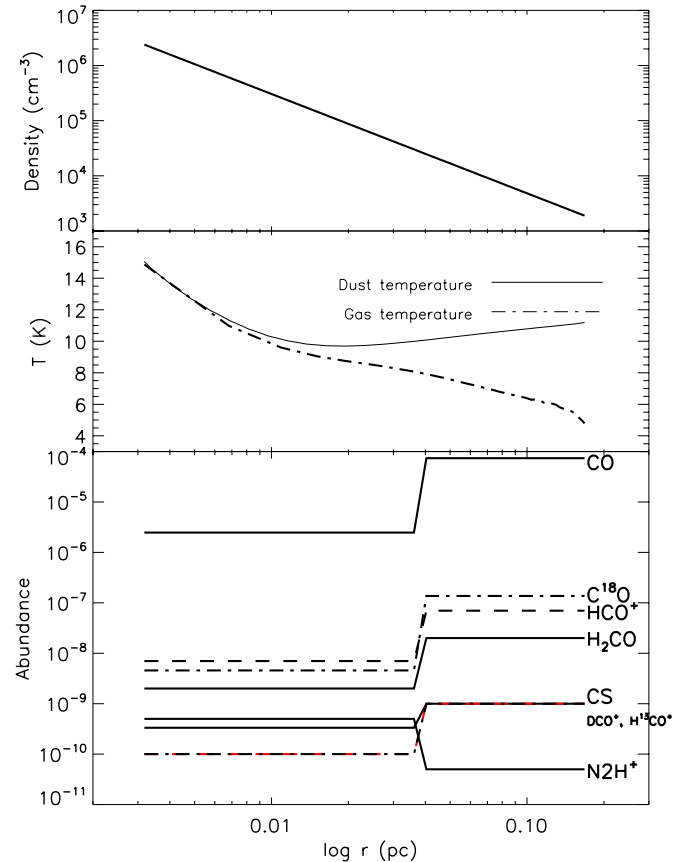

Figure 13. First panel is the density profile as a function of radius, which follows $n(r) \propto r^{-1.8}$. The second panel is the gas and dust temperature distribution as a function of radius. The solid line is the dust temperature and the dash-dotted line is the gas temperature profile. The dust temperature and the gas temperature are almost the same in the inner region due to the high collision rate, because of the high density in the inner part. In the outer part of the cloud, the gas temperature is lower than the dust temperature, since the photoelectric heating is too low to heat the gas. The last panel shows the step function abundance profiles as a function of radius. The molecules freeze out in the inner part of the cloud. Since CO destroys the N_2H^+ molecule, the abundance profile of N_2H^+ has a reversed shape from other molecules.

(A color version of this figure is available in the online journal.)

and the disk scale height is given as

$$\frac{H_p(R)}{R} = \frac{H_{\mathrm{disk}}}{R_{\mathrm{disk}}}\left(\frac{R}{R_{\mathrm{disk}}}\right)^{\alpha_{\mathrm{fl}}}. \qquad (3)$$

We set the disk outer radius as 350 AU, which is the inner radius of the envelope. The disk inner radius is 0.03 AU, set to the location at which a dust temperature is 1500 K. We use most of the other disk model parameters in Whitney et al. (2003). The flaring index α_{fl} is set to 0.25, and the surface density power-law index is set to $p = 1$. The disk mass is set as $M_{\mathrm{disk}} = 0.01\,M_\odot$.

We ran a grid of models varying three free parameters to fit the observed SED. As for the 1D models, we calculated χ^2 for the photometric points to determine the best fit. The free parameters are the disk scale height, $H_{\mathrm{disk}}/R_{\mathrm{disk}}$ at $R_{\mathrm{disk}} = 100$ AU, the internal luminosity, L_{int}, and the inclination angle. Again, we plot the χ^2 versus the free parameter, setting the other two free parameters at particular values. Panel (a) of Figure 11 presents χ^2 with the disk scale height $H_{\mathrm{disk}}/R_{\mathrm{disk}}$ varying in the range between 0.01 (Whitney et al. 2003) and 0.125 (Pontoppidan et al. 2007b). The best fit occurs for $H_{\mathrm{disk}}/R_{\mathrm{disk}} = 0.05 \pm 0.005$. Panel (b) in Figure 11 is the χ^2 versus internal luminosity.
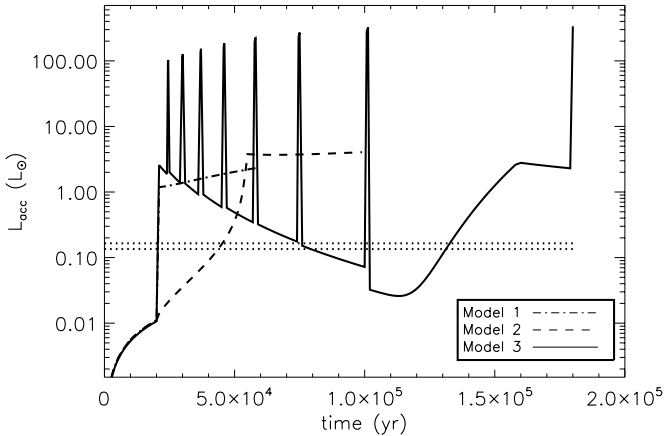
Figure 14. Luminosity evolution of the models we have used for chemical evolution. The dash-dotted line is Model 1 (Young & Evans 2005), the dashed line is Model 2 (Lee et al. 2004), and the solid line is Model 3 (Dunham et al. 2010a). The early stage evolution is the same in all three models. The two horizontal lines indicate the best-fit luminosities for 1D and 2D models.

Since the disk is now heated only from the reprocessing of the central star, the internal luminosity affects the SED mostly in the MIR. If the internal luminosity is low, it cannot heat the disk enough. If L_{int} is high, the modeled SED becomes stronger than the observed flux density everywhere. The best fit is at $L_{int} = 0.14 \pm 0.005\,L_{\odot}$, which is a little bit lower than that found for the 1D model ($0.16\,L_{\odot}$). Panel (c) is the χ^2 plot as a function of the inclination angle. The inclination angle affects the MIR SED, since the inclination angle affects the disk emission. There is a broad minimum in χ^2 around an inclination angle of 70°, but the SED for the model at 70° badly underestimates the observations at $24\,\mu$m, which are well fitted by a model with an inclination angle of 50°, which however badly overestimates the observations at $70\,\mu$m. The SEDs with these two inclination angles are plotted in Figure 12. Neither model matches all of the IRS spectrum either. In particular, the observed CO_2 feature is deeper than produced by any of the models.

The best-fit parameters are summarized in Table 6. The internal luminosity from the 1D model is $0.16\,L_{\odot}$, the internal luminosity from the 2D model is $0.14\,L_{\odot}$. Both luminosities are slightly higher than the VeLLO criterion ($L_{int} = 0.1\,L_{\odot}$). CB130-1-IRS1 is a low-luminosity source, but not a VeLLO.

6. MOLECULAR LINE MODEL

Chemical modeling of the line observations is needed to determine the chemical properties of the source. We found that the chemical properties can give further clues to the evolutionary state of the source. In this section, we use step-function models of the chemical abundances, which will provide a simple comparison to the full chemical models employed in the following section.

Because the chemical models are not very sensitive to the 2D structure of the source, we use 1D models of the dust. For each chemical model, we first calculate the dust radiative transfer to get the dust temperature distribution. Next, we calculate the gas kinetic temperature (Section 6.1), and then use step function abundance models, which can give a reasonable fit to the observed molecular lines (Lee et al. 2003; Evans et al. 2005; Section 6.2). An MC code (Choi et al. 1995) calculates the molecular excitation and a virtual telescope (VT) simulation produces line profiles, which can be compared to the observed

Table 6
Best-fit Model Parameters of CB130-1

Parameter	One Dimensional	Two Dimensional
Stellar temperature	3000 K	. . .
Internal luminosity	$0.16 \pm 0.005\,L_{\odot}$	$0.14 \pm 0.005\,L_{\odot}$
Inner radius	350 AU	. . .
Inclination angle	. . .	50°–70°
Disk scale height	. . .	0.05 ± 0.005

lines (Section 6.3). Comparing observations to line profiles predicted from empirical abundance profiles can constrain the abundance profiles.

6.1. Gas Temperature

We calculate the radial gas temperature distribution using a gas energetics code (Doty & Neufeld 1997; Young et al. 2004b), which includes energy transfer between gas and dust, heating by cosmic rays, photoelectric heating, and molecular cooling.

The collision rate between gas and dust depends on the cumulative grain cross section. In this simulation, the grain cross section per baryon is 6.09×10^{-22} cm^2 (Young et al. 2004b), based on the OH5 model. This is slightly different from the opacity model we have used for DUSTY modeling, but the line modeling does not critically depend on the opacity model. We take the cosmic ray ionization rate as 3.0×10^{-17} s^{-1} (Roberts & Herbst 2002; van der Tak & van Dishoeck 2000).

The photoelectric heating is determined by the strength of the UV part of the ISRF and the electron number density. The electron number density is assumed to be 0.001 cm^{-3} (Doty et al. 2002). The CO line shows stronger emission when the envelope is heated by the unattenuated ISRF. So we vary the extinction of the ISRF by the surrounding material until it reproduces the observed CO line. See Evans et al. (2005) for a full explanation of this method. The relevant part of the ISRF for the gas heating is in the FUV, where the ISRF is characterized by G_0. Assuming a plane parallel slab, the ISRF is attenuated following $G_0 = G(\mathrm{ISM})e^{-\tau_{UV}}$, where $G(\mathrm{ISM})$ is the unattenuated FUV field. The best match to the observed CO line requires $G_0/G(\mathrm{ISM}) = 4.5 \times 10^{-3}$. The relation between optical depth in the UV band and the V band is $\tau_{UV} = 1.8 A_V$. Thus, we attenuate the ISRF at the outer boundary of the envelope by $A_V = -0.56\ln(4.5 \times 10^{-3}) = 3$. We used this value for the external attenuation of the ISRF in Section 5.1. Of course, the FUV is further attenuated as it propagates into the cloud, and the model accounts for this.

The cooling rate mainly depends on the abundance and the line width of CO. We set the CO fractional abundance relative to H$_2$ to be 7.4×10^{-5} (Bacmann et al. 2002; Jørgensen et al. 2002). We use a Doppler $b = 0.8$ km s^{-1}, which fits best the CO molecular line.

The calculated gas temperature is plotted in the middle panel of Figure 13, along with the dust temperature. The dust temperature and gas temperature are almost the same in the inner region due to the high gas–dust collision rate because of the high density in the inner region, shown in the upper panel. In the outer part of the cloud, the gas temperature is lower than the dust temperature, because the gas temperature has decoupled from the dust temperature and the photoelectric heating from the attenuated ISRF is too low to heat the gas.
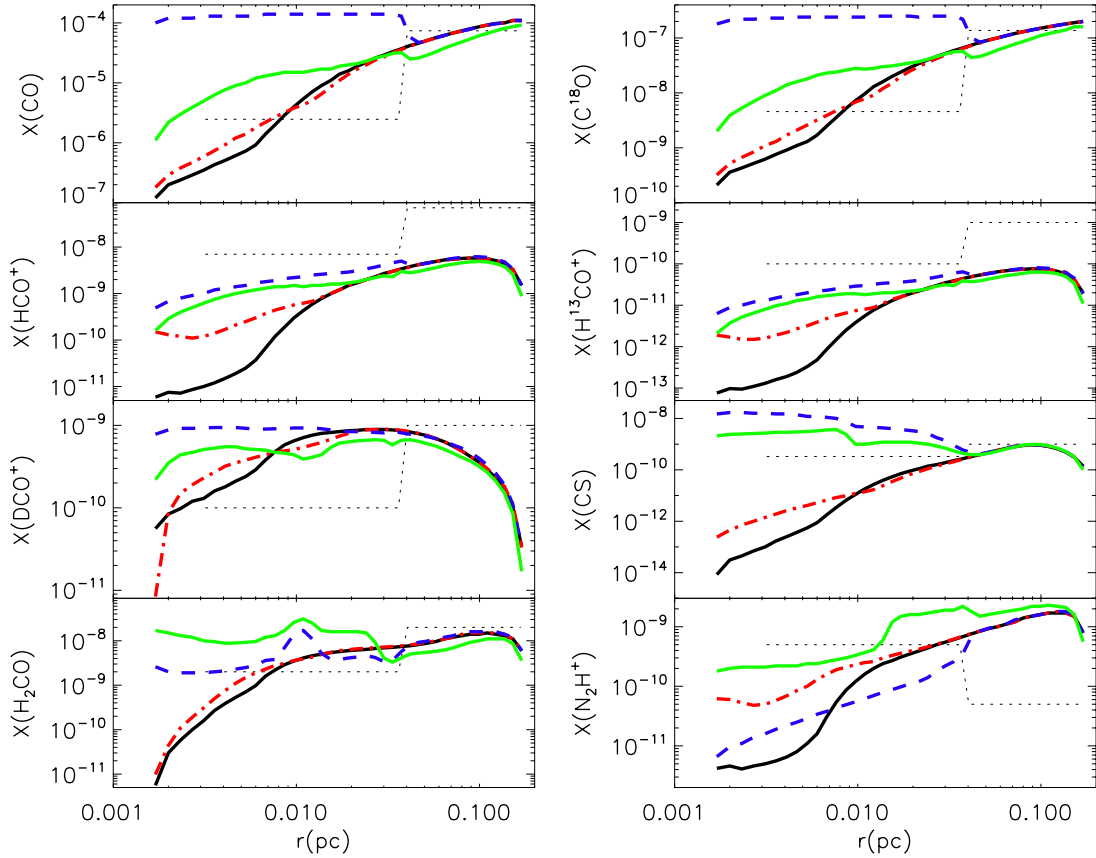
Figure 15. Abundance profiles with Model 1, Model 2, Model 3, Model 4, and the step function abundances for comparison. The abundance profiles with Model 1 at 20,000 years are plotted in solid lines. The abundance profiles from Model 2 at 36,000 years are plotted in dash-dotted lines. The abundance profiles from Model 3 at 78,000 years are plotted in dashed lines. The triple-dot-dashed lines are the abundance profiles of Model 4. For comparison, we plotted the best-fit step function abundances in thin dotted lines. The chemical modeled abundance profiles are in the range of the step function abundances except for HCO^+ and $H^{13}CO^+$.

(A color version of this figure is available in the online journal.)

6.2. Abundance Profile

We use step function abundance profiles. Molecules tend to freeze out onto the grain surfaces in cold and dense regions. The inner part of the cloud has higher density compared to the outer region, so molecules freeze out faster. If the dust temperature becomes high enough, the molecules will sublimate. The CO sublimation temperature is about 20 K. The highest temperature in the model cloud is less than 20 K in the innermost region of the envelope, 0.003 pc, since CB130-1-IRS1 is a low-luminosity source. The dust temperature is too low to sublimate the frozen-out CO. In the outermost part, the density is too low for significant freeze-out. Thus, a step function is a reasonable profile for the cloud. The three parameters of the abundance profile are the undepleted abundance (X_0), depletion radius (r_D), and depletion fraction (f_D). The best-fitting parameters are summarized in Table 7. The abundance profiles are plotted in the last panel in Figure 13.

6.3. Monte Carlo Simulation

The line profiles are modeled with the MC code (Choi et al. 1995) to calculate level populations of molecules. The MC code can handle arbitrary 1D distributions of the systematic velocity, the density, the kinetic temperature, the microturbulence, and the abundance self-consistently.

Infalling envelopes sometimes exhibit a stronger blue wing for optically thick lines with a substantial excitation temperature gradient (Evans 1999; Lee et al. 2007). Even though CB130-1

Table 7
Best-fitting Step Function Abundance Parameters

Line	X_0	r_D (pc)	f_D
CO	7.40×10^{-5}	0.04	30
$C^{18}O$	1.37×10^{-7}	0.04	30
HCO^+	7.00×10^{-8}	0.04	10
$H^{13}CO^+$	1.00×10^{-9}	0.04	10
DCO^+	1.00×10^{-9}	0.04	10
N_2H^+	5.00×10^{-10}	0.04	0.1
CS	1.00×10^{-9}	0.04	3
H_2CO	2.00×10^{-8}	0.04	10

Note. The free-parameter values of the step function abundance profiles obtained with the line modeling.

contains a protostar, there is no significant feature of infall in molecular lines. All lines show a single peak, so we do not include any systematic velocity in the models.

Doppler b parameters are determined by the width of each line. We have used $b = 0.8$ km s^{-1} for CO. Since the CO line is optically thick and dominated by the outer part of the envelope, the CO line is difficult to fit with the same Doppler b parameter as others. We used $b = 0.2$ km s^{-1} for all the other lines, based on the widths of relatively optically thin lines, such as $C^{18}O$ and $H^{13}CO$.

After MC modeling, a VT program is used to integrate the emission along the line of sight and to match the velocity and
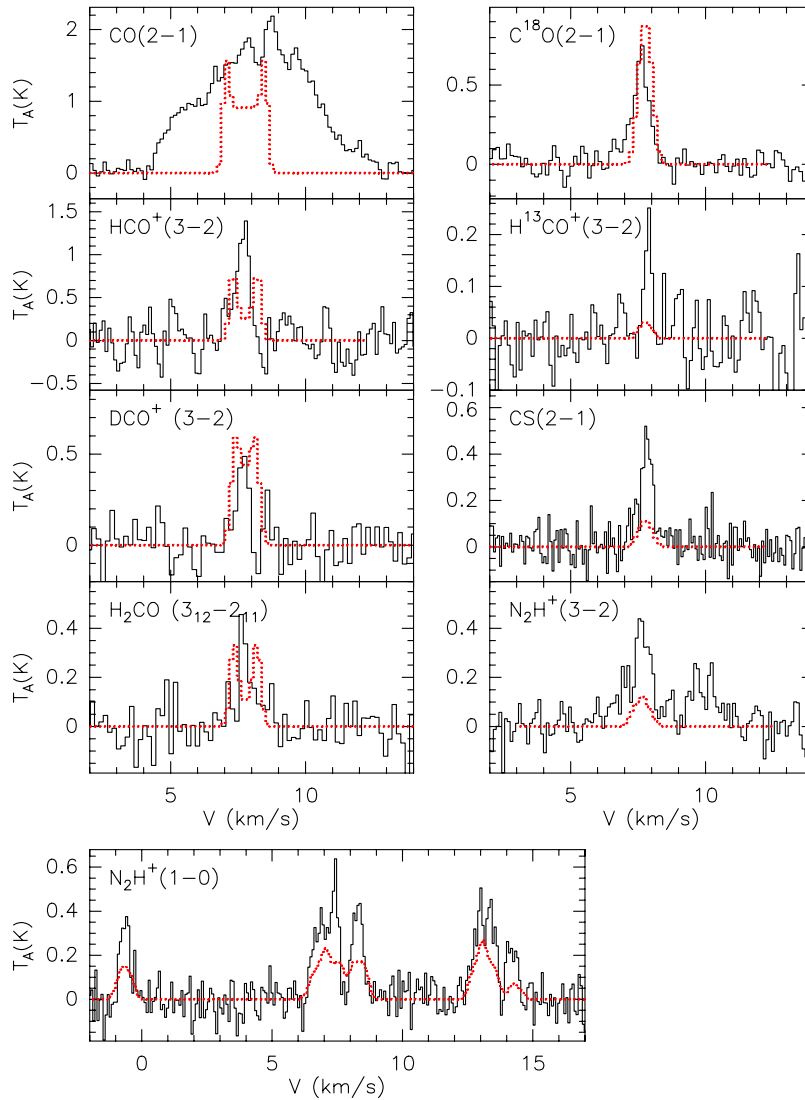
Figure 16. Molecular lines from the chemical evolution model with Model 1. The solid lines are the observed molecular lines and the dotted lines are modeled molecular lines. The time is 20,000 years with luminosity 0.011 $L_\odot$, which is just before the FHSC stage ends.

(A color version of this figure is available in the online journal.)

spatial resolutions, as well as the beam efficiency. All lines are assumed to be centered at 7.77 km s^{-1}, determined by averaging the LSR velocity of optically thin lines.

By comparing modeled spectra to observations, we can estimate the abundance. The best-fit abundances are given in Table 7. We set the depletion radius as 0.04 pc. We used the isotope ratio for the low-mass protostellar envelope described in Jørgensen et al. (2004). The ratio of O to ^{18}O is 540, and the ratio between C and ^{13}C is 70. CO destroys N$_2$H$^+$ molecules, so N$_2$H$^+$ has a reverse abundance profile compared to the CO abundance. The N$_2$H$^+$ line has a hyperfine structure. The MC code calculates line modeling for each hyperfine line, and then they are added together.

The best-fit results are shown in Figure 7. The modeled C^{18}O, CS, and N$_2$H$^+$ ($J = 1 \rightarrow 0$) lines show reasonable fits to the observed lines, while modeled CO and HCO$^+$ lines show a poor fit with the observed lines. The strengths are in a reasonable range for both HCO$^+$ and H^{13}CO$^+$, but the abundance that fits the observed H^{13}CO$^+$ line produces a self-reversed feature in the modeled HCO$^+$ line. The modeled HCO$^+$ has a low excitation temperature in the outer region, so it shows absorption features

at the center of the line. However, the observed HCO$^+$ line does not show a self-reversed structure. The modeled H$_2$CO also shows a self-reversed structure. The prediction of self-reversed lines that are not observed is a common problem (Carr et al. 1995; Chen et al. 2009), and it suggests that macroturbulent and clumpy three-dimensional models would be more appropriate. Though modeled DCO$^+$, CS, and N$_2$H$^+$ ($J = 3 \rightarrow 2$) line strengths are weaker than the observed lines, the difference is less than a factor of 2.5.

7. CHEMO-DYNAMICAL MODELS

7.1. Chemical Models with Luminosity Evolution Scenarios

CB130-1 is a low-luminosity source. There is no significant evidence of a CO outflow, but there is a reflection nebula suggestive of an outflow cavity. CB130-1 could be in the first hydrostatic core (FHSC) stage or in a quiescent stage between episodic accretion bursts. With chemical evolution modeling, we may be able to distinguish these possibilities. Because it takes time to relax the chemistry in the core, evidence of a past high-luminosity stage might be present in the abundances.
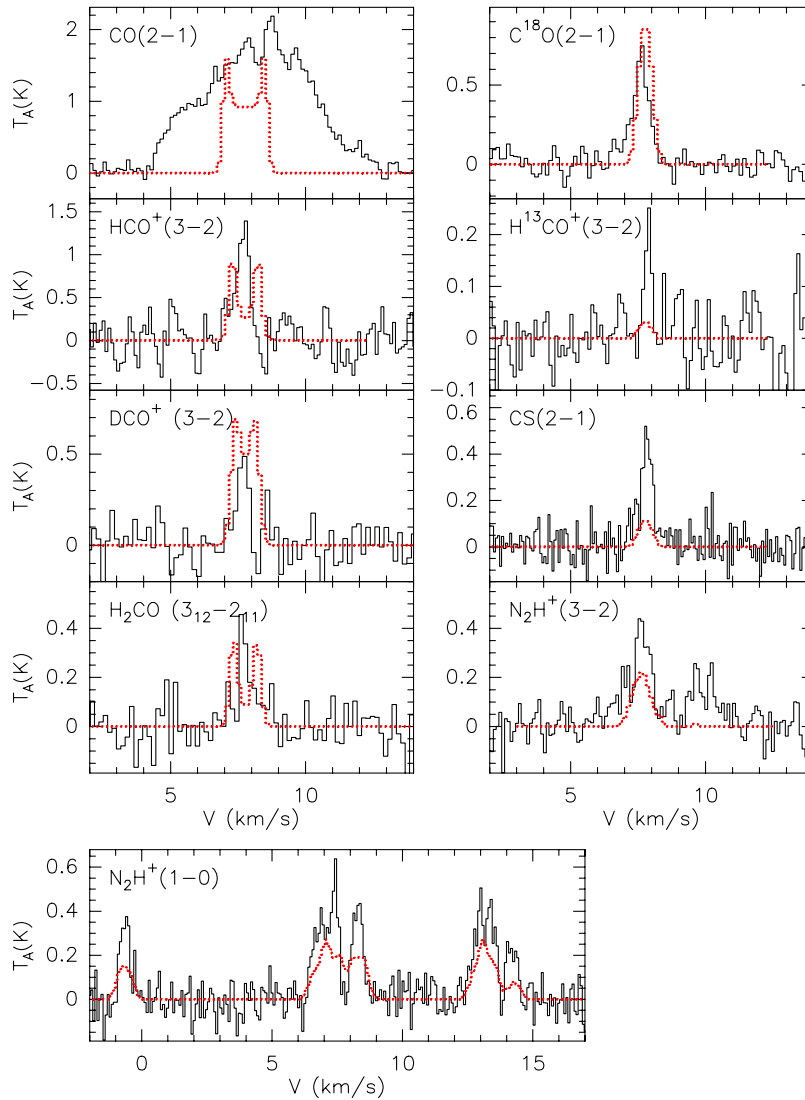
Figure 17. Molecular lines from Model 2. The solid lines are the observed molecular lines and the dotted lines are modeled molecular lines. This model includes a long FHSC transition stage. The time is 45,000 years with the internal luminosity $0.16\,L_\odot$.

(A color version of this figure is available in the online journal.)

We use the evolutionary chemo-dynamical model by Lee et al. (2004) to test this idea. This model calculates the chemical evolution of a core from the prestellar core to the embedded protostellar core stage. At each time step, the density profile, the dust temperature, the gas temperature, and abundances are calculated self-consistently.

At the prestellar stage, the density distribution is described by a sequence of Bonnor–Ebert spheres. We adopt the time duration at the preprotostellar core stage in Table 4 in Chen et al. (2009), which has a longer total timescale at the prestellar stage. Once a singular isothermal sphere has been reached with $n(r) \propto r^{-2}$, the inside-out collapse is initiated, and $n(r)$ approaches $r^{-1.5}$ inside the infall radius. The infall radius propagates outward at the sound speed through the envelope.

We use three kinds of luminosity evolution models in the accretion stage. First, in Model 1, we adopt the accretion luminosity from Young & Evans (2005) including the FHSC stage (Larson 1969; Boss 1993; Masunaga et al. 1998). The FHSC represents the core in an initial quasi-static contraction stage when it is still molecular. When the core temperature reaches 2000 K, the molecular hydrogen dissociates, so the core

has a second collapse and the FHSC stage ends. Models indicate that the FHSC has a short, but poorly determined, lifetime, about 10^4 years (Boss & Yorke 1995; Masunaga et al. 1998), a very low luminosity, and a high optical depth. While two candidates have recently been proposed (Chen et al. 2010; Enoch et al. 2010), the FHSC has not yet been clearly detected. In Model 1, the FHSC lasts 20,000 years and the collapse of the FHSC occurs in 100 years. When $t = 20,000$ years, $L_{acc} \sim 0.011\,L_\odot$, which is only 10% of the internal luminosity of CB130-1-IRS1. The luminosity increases rapidly after 20,000 years. We adopt a time at the very end of the FHSC stage of Model 1, which has a luminosity much lower than that of CB130-1-IRS1. To match the luminosity of the object, we would have to be catching the source in an extremely short-lived phase while the FHSC is collapsing.

The luminosity evolution of Model 2 is taken from Lee et al. (2004). In Model 2, the FHSC lasts 20,000 years and the transition occurs in 32,000 years, providing a better chance to see a source with the observed luminosity. However, this longer transition stage has no particular theoretical justification. Here, we choose 45,000 years as our desired time since L_{acc} is $0.16\,L_\odot$ at that time.
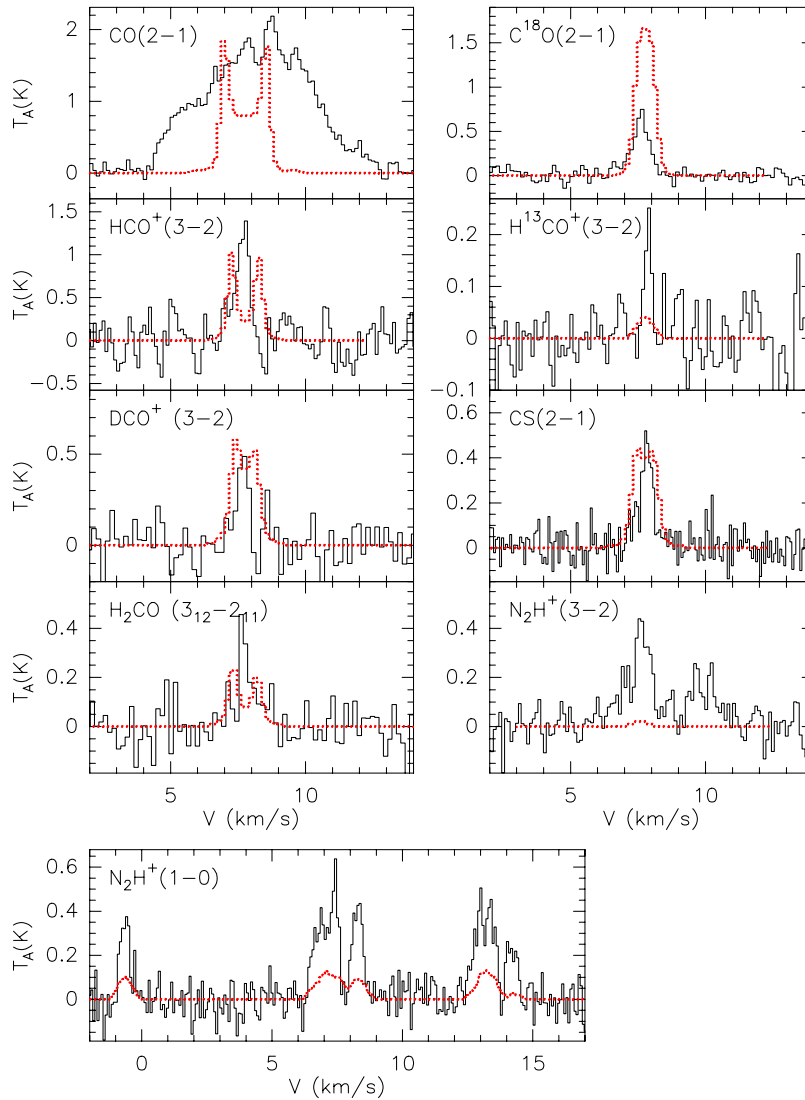
Figure 18. Molecular line result at 78,000 years with Model 3. The solid lines are observed molecular lines, and the dotted lines are the modeled lines at 78,000 years of Model 3. The internal luminosity at this stage is 0.14 $L_\odot$. It has gone through six periods of accretion bursts, and 3000 years have passed after the accretion burst. The modeled $C^{18}O$ is stronger and the modeled N_2H^+ is weaker than the observed lines.

(A color version of this figure is available in the online journal.)

The last model of luminosity evolution, Model 3, uses the episodic accretion luminosity model from Dunham et al. (2010a). The episodic accretion is included in a simple, idealized way rather than in a self-consistent model. The model assumes no accretion from disk to star most of the time, but continued infall from envelope to disk. A mass accretion burst occurs when the disk mass reaches 0.2 times the stellar mass. Then mass accretion from the disk to protostar increases to $\dot{M} = 1 \times 10^{-4}\,M_\odot\mathrm{yr}^{-1}$, which is about 100 times the average mass accretion rate. The accretion luminosity depends on $\dot{M}$, so the accretion luminosity also evolves episodically. The envelope mass of CB130-1 is 5.3–5.5 $M_\odot$. So among the three masses in Dunham et al. (2010a), a 3 $M_\odot$ envelope model is the closest. However, the luminosity evolution of the model with a 3 $M_\odot$ envelope never falls below 1 $L_\odot$ after the FHSC stage ends, so we take the luminosity evolution of the 1 $M_\odot$ envelope model in Dunham et al. (2010a). In Model 3, we adopt 78,000 years as our desired time step. At 78,000 years, the internal luminosity is 0.14 $L_\odot$. The cloud has gone through six burst episodes, and 3000 years have passed after the sixth burst. The luminosity

evolution of the three models are plotted in Figure 14. The early stage evolution is the same in all three models. After 20,000 years, Model 2 has the lowest luminosity among the three models.

We calculate the dust temperature distribution with DUSTY at each time step. We use the same parameters described in Section 5.1. Then we calculate the gas temperature considering the parameters described in Section 6.1. The chemical evolution is calculated for each of the 512 gas parcels as it falls into the central region. Gas inside the infall radius carries the memory of the conditions from farther out. The chemical calculation includes interactions between gas and dust grains and gas-phase reactions, but does not include chemical reactions on grain mantles explicitly. We assume the surface binding energy of species onto bare SiO_2 dust grains. We use an updated chemical network with a new binding energy of N_2 and deuterated species, which is used in Chen et al. (2009).

The abundance profile at each time step is calculated through the chemical evolution model. We use the same isotope ratio as in Section 6.3. The abundance profiles are plotted in Figure 15.
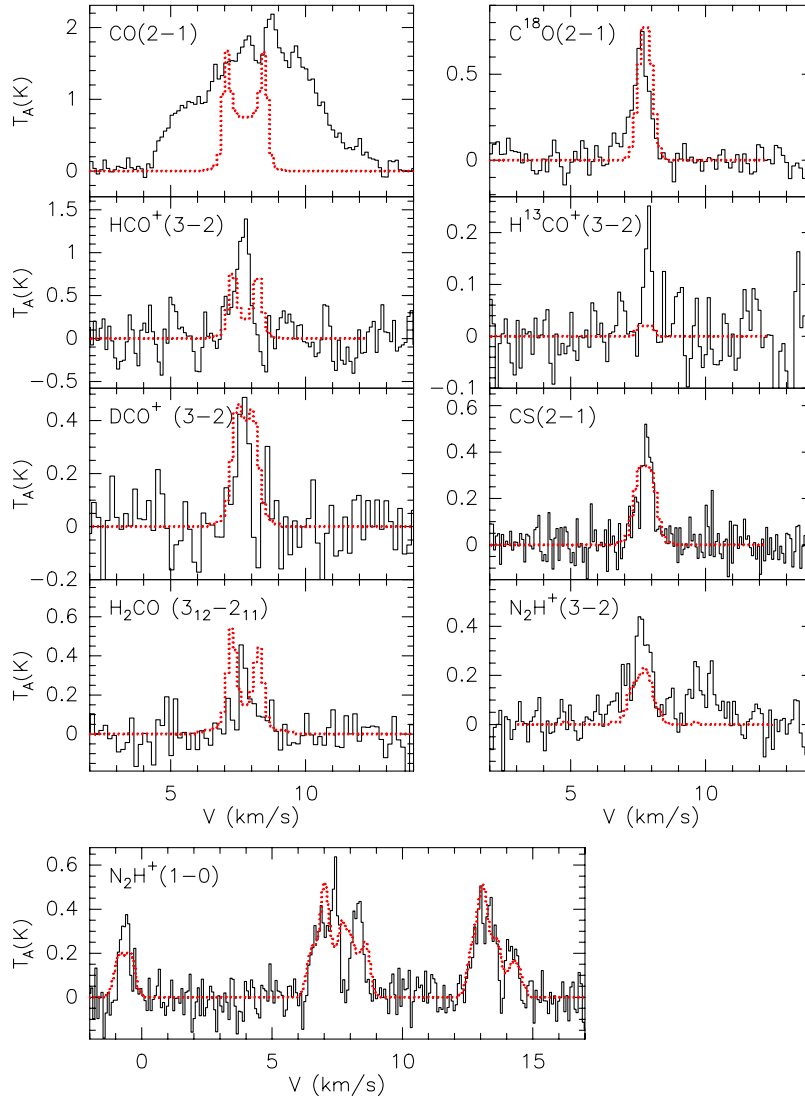
Figure 19. Molecular line result with Model 4. The solid lines are observed molecular lines, and the dotted lines are the modeled lines. The evolution stage is the same as Model 3. The calculation turned 80% of CO ice into CO_2 ice during low-luminosity periods. The lines of $C^{18}O$, CS, DCO^+, H_2CO, and N_2H^+ are fitted better than in the other models.

(A color version of this figure is available in the online journal.)

The abundance profiles of Model 1 and Model 2 do not have a CO evaporation region at the center. In both cases, the central source has a low luminosity, and it does not heat the envelope enough to make CO sublimate. Model 2 has higher abundances compared to Model 1, except for DCO^+. In Model 3, the abundances of CO and $C^{18}O$ show the CO sublimation region at the central region because of past periods of high luminosity. The modeled abundances of HCO^+, $H^{13}CO^+$ are all low compared to the best-fit step function abundances.

Once all the physical parameters are determined, we use MC code (Choi et al. 1995) to calculate the level populations. Then we use VT code to produce line profiles. The molecular line profiles with Model 1 are plotted in Figure 16, and with Model 2 in Figure 17. The modeled lines of HCO^+, $H^{13}CO^+$, CS, and N_2H^+ are weaker than the observed lines, and the DCO^+ line is stronger than the observed line. N_2H^+ shows a better fit with Model 2, but the $J = 3 \rightarrow 2$ line is still weak. The molecular lines with Model 3 are plotted in Figure 18. In Model 3, the $C^{18}O$ line is much stronger than observed lines. On the other hand, HCO^+, $H^{13}CO^+$, and N_2H^+ are weaker than observed lines. The

modeled N_2H^+ (3–2) line is very weak. All three models show strong $C^{18}O$ and weak N_2H^+ lines compared to the observed lines. The modeled $C^{18}O$ is much stronger in Model 3, because the episodic bursts have sublimated the CO in the inner region. The N_2H^+ line is weak in all three models.

All the models have caveats in their luminosity evolution scenarios. Model 1 does not actually match the observed $L_{int} \sim 0.14$–$0.16\,L_\odot$. Model 2 assumes that the transition stage of FHSC lasts for 32,000 years, which is unrealistic. It can give a source luminosity of $0.16\,L_\odot$, and gives a slightly better fit to the $C^{18}O$ and N_2H^+ compared to Model 1. However, the modeled DCO^+ line is too strong, and the modeled CS line is too weak. In Model 3, the envelope mass is lower than our estimates for CB130-1. Also, the best-fit TSC model density from the 2D model is 35,000 years, while the desired luminosity of Model 3 is reached at $t = 78,000$ years, which means that more envelope material from Model 3 has already fallen in. The problems with the luminosity evolution scenarios show how chemical modeling can provide additional constraints that are distinct from those from modeling the continuum.

7.2. Including the Conversion of CO into CO$_2$ Ice

We have one more trick to try. As noted in Section 4.2, a substantial amount of carbon is contained in CO_2 ice. Once CO freezes out onto dust grain surfaces, a fraction of CO ice turns into CO_2 ice (Pontoppidan et al. 2007a). CO_2 ice does not sublimate during the accretion burst even when the CO evaporation temperature is reached. So the amount of CO returned to the gas phase is less than the amount of CO frozen onto grain surfaces during the quiescent phase. The net effect is to decrease gas phase CO and enhance N_2H^+. We used the same episodic accretion luminosity evolution model as Model 3, and varied the fraction of CO ice which turns into CO_2 ice in the chemical network (Model 4). When 80% of CO ice turns into CO_2 ice, the modeled $C^{18}O$ and N_2H^+ lines match well with the observed lines. Also, DCO^+ and CS fit the data better than in Model 3. The abundance of this model is plotted in Figure 15 and the molecular line profiles are plotted in Figure 19. The CO_2 ice column density obtained from the best-fit model is 2.94×10^{18} cm^{-2}, 1.1 times observed value, within the likely range of systematic uncertainties.

Among the models, the episodic model including CO_2 ice formation fits best to the observed lines in all molecules. Based on the modeling result, we suggest that CB130-1 has gone through episodic accretion, forming CO_2 ice out of CO ice in quiescent phases. This model can explain the low luminosity of the source, the strong CO_2 ice feature, and most of the gas phase emission lines. There are still inconsistencies in this model, so further development of episodic accretion models is needed.

8. SUMMARY

We presented a detailed study of a low-luminosity object in the CB130-1 region. We performed radiative transfer modeling and chemical modeling to explain the core with a low-luminosity protostar in it.

The embedded protostar CB130-1-IRS1 has $L_{int} = 0.14\,L_\odot$ (1D model) to $L_{int} = 0.16\,L_\odot$ (2D model). This is a slightly higher luminosity than a VeLLO has, but still CB130-1-IRS1 is a low-luminosity source at about 0.1 of the expected luminosity for steady accretion onto an object at the boundary between stars and brown dwarfs.

We tested both a step function abundance model and self-consistent chemical evolution models. The step function abundance profile fits observed lines reasonably well, but is of course, ad hoc. For the self-consistent models, we use three different luminosity evolution scenarios to explain the low luminosity of the object. All three luminosity evolution models with the standard chemical network show that the modeled $C^{18}O$ line is strong and N_2H^+ is weak compared to the observations. The step function model has more free parameters than the chemical evolution model, so it is more feasible to fit the observed lines.

The deep 15.2 μm CO_2 ice feature indicates that CO_2 ice has formed from CO ice. We added a reaction to the chemical network, which turns CO ice into CO_2 ice. A model with that reaction decreases the $C^{18}O$ abundance and increases the N_2H^+ abundance. With the episodic accretion model and the modified network, we can explain the low luminosity of the source, the strong CO_2 ice feature, and most of the gas phase emission lines at the same time. So, CB130-1 is most likely neither an FHSC nor a very low mass object, but a more evolved protostar in a quiescent stage between accretion bursts. With further study of CO_2, CO, and N_2H^+ in low-luminosity objects, we may find chemical imprints of episodic accretion in low-luminosity objects.

REFERENCES

Allen, L. E., et al. 2004, ApJS, 154, 363
André, P., Motte, F., & Bacmann, A. 1999, ApJ, 513, L57
Bacmann, A., et al. 2002, A&A, 389, L6
Boss, A. P. 1993, ApJ, 410, 157
Boss, A. P., & Yorke, H. W. 1995, ApJ, 439, L55
Bourke, T. L., et al. 2006, ApJ, 649, L37
Butner, H. M., Natta, A., & Evans, N. J., II. 1994, ApJ, 420, 326
Carr, J. S., Evans, N. J., II, Lacy, J. H., & Zhou, S. 1995, ApJ, 450, 667
Chen, H., Myers, P. C., Ladd, E. F., & Wood, D. O. S. 1995, ApJ, 445, 377
Chen, J.-H., Evans, N. J., Lee, J.-E., & Bourke, T. L. 2009, ApJ, 705, 1160
Chen, X., et al. 2010, ApJ, 715, 1344
Chiang, E. I., & Goldreich, P. 1997, ApJ, 490, 368
Choi, M., Evans, N. J., II, Gregersen, E. M., & Wang, Y. 1995, ApJ, 448, 742
Clemens, D. P., & Barvainis, R. 1988, ApJS, 68, 257
Dame, T. M., & Thaddeus, P. 1985, ApJ, 297, 751
di Francesco, J., Evans, N. J., II, Caselli, P., Myers, P. C., Shirley, Y., Aikawa, Y., & Tafalla, M. 2007, in Protostars and Planets V, ed. B. Reipurth, D. Jewitt, & K. Keil (Tucson, AZ: Univ. Arizona Press), 17
Doty, S. D., & Neufeld, D. A. 1997, ApJ, 489, 122
Doty, S. D., van Dishoeck, E. F., van der Tak, F. F. S., & Boonman, A. M. S. 2002, A&A, 389, 446
Dullemond, C. P., & Dominik, C. 2004, A&A, 417, 159
Dullemond, C. P., Dominik, C., & Natta, A. 2001, ApJ, 560, 957
Dunham, M. M., Evans, N. J., Terebey, S., Dullemond, C. P., & Young, C. H. 2010a, ApJ, 710, 470
Dunham, M. M., et al. 2006, ApJ, 651, 945
Dunham, M. M., et al. 2008, ApJS, 179, 249
Dunham, M. M., et al. 2010b, ApJ, 721, 995
Enoch, M. L., Evans, N. J., Sargent, A. I., & Glenn, J. 2009, ApJ, 692, 973
Enoch, M. L., Lee, J., Harvey, P., Dunham, M. M., & Schnee, S. 2010, ApJ, 722, L33
Evans, N. J., II. 1999, ARA&A, 37, 311
Evans, N. J., II, Lee, J.-E., Rawlings, J. M. C., & Choi, M. 2005, ApJ, 626, 919
Evans, N. J., II, Rawlings, J. M. C., Shirley, Y. L., & Mundy, L. G. 2001, ApJ, 557, 193
Evans, N. J., II, et al. 2003, PASP, 115, 965
Evans, N. J., II, et al. 2007, Final Delivery of Data from the c2d Legacy Project: IRAC and MIPS (Pasadena, CA: Spitzer Science Center)
Evans, N. J., et al. 2009, ApJS, 181, 321
Fazio, G. G., et al. 2004, ApJS, 154, 10
Gerakines, P. A., Schutte, W. A., Greenberg, J. M., & van Dishoeck, E. F. 1995, A&A, 296, 810
Gordon, K. D., et al. 2005, PASP, 117, 503
Greene, T. P., Wilking, B. A., Andre, P., Young, E. T., & Lada, C. J. 1994, ApJ, 434, 614
Gutermuth, R. A., et al. 2004, ApJS, 154, 374
Harvey, P., et al. 2007, ApJ, 663, 1149
Houck, J. R., et al. 2004, ApJS, 154, 18
Huard, T. L., et al. 2006, ApJ, 640, 391

Ivezic, Z., Nenkova, M., & Elitzur, M. 1999, arXiv:astro-ph/9910475
Jørgensen, J. K., Schöier, F. L., & van Dishoeck, E. F. 2002, A&A, 389, 908
Jørgensen, J. K., Schöier, F. L., & van Dishoeck, E. F. 2004, A&A, 416, 603
Kauffmann, J., Bertoldi, F., Evans, N. J., II, & the C2D Collaboration. 2005, Astron. Nachr., 326, 878
Kenyon, S. J., Hartmann, L. W., Strom, K. M., & Strom, S. E. 1990, AJ, 99, 869
Lahuis, F., et al. 2006, c2d Spectroscopy Explanatory Supplement (Pasadena, CA: Spitzer Science Center)
Landsman, W. B. 1993, in ASP Conf. Ser. 52, Astronomical Data Analysis Software and Systems II, ed. R. J. Hanisch, R. J. V. Brissenden, & J. Barnes (San Francisco, CA: ASP), 246
Larson, R. B. 1969, MNRAS, 145, 271
Launhardt, R., et al. 2010, ApJS, 188, 139
Lee, C. W., & Myers, P. C. 1999, ApJS, 123, 233
Lee, C. W., et al. 2009, ApJ, 693, 1290
Lee, J.-E. 2007, J. Korean Astron. Soc., 40, 85
Lee, J.-E., Bergin, E. A., & Evans, N. J., II. 2004, ApJ, 617, 360
Lee, J.-E., Di Francesco, J., Bourke, T. L., Evans, N. J., II, & Wu, J. 2007, ApJ, 671, 1748
Lee, J.-E., Evans, N. J., II, Shirley, Y. L., & Tatematsu, K. 2003, ApJ, 583, 789
Masunaga, H., Miyama, S. M., & Inutsuka, S. 1998, ApJ, 495, 346
Myers, P. C., & Ladd, E. F. 1993, ApJ, 413, L47

Ossenkopf, V., & Henning, T. 1994, A&A, 291, 943
Pontoppidan, K. M., et al. 2007a, ApJ, 656, 980
Pontoppidan, K. M., et al. 2007b, ApJ, 656, 991
Rieke, G. H., et al. 2004, ApJS, 154, 25
Roberts, H., & Herbst, E. 2002, A&A, 395, 233
Shirley, Y. L., Evans, N. J., II, & Rawlings, J. M. C. 2002, ApJ, 575, 337
Shirley, Y. L., Evans, N. J., II, Rawlings, J. M. C., & Gregersen, E. M. 2000, ApJS, 131, 249
Shu, F. H. 1977, ApJ, 214, 488
Straižys, V., Černis, K., & Bartašiūtė, S. 2003, A&A, 405, 585
Stutz, A. M., et al. 2007, ApJ, 665, 466
Terebey, S., Shu, F. H., & Cassen, P. 1984, ApJ, 286, 529
van der Tak, F. F. S., & van Dishoeck, E. F. 2000, A&A, 358, L79
Whitney, B. A., Wood, K., Bjorkman, J. E., & Wolff, M. J. 2003, ApJ, 591, 1049
Wu, J., Dunham, M. M., Evans, N. J., II, Bourke, T. L., & Young, C. H. 2007, AJ, 133, 1560
Young, C. H., & Evans, N. J., II. 2005, ApJ, 627, 293
Young, C. H., Shirley, Y. L., Evans, N. J., II, & Rawlings, J. M. C. 2003, ApJS, 145, 111
Young, C. H., et al. 2004a, ApJS, 154, 396
Young, K. E., Lee, J., Evans, N. J., II, Goldsmith, P. F., & Doty, S. D. 2004b, ApJ, 614, 252